iScience

CellPress
OPEN ACCESS

Article

Targeting endometrial inflammation in intrauterine adhesion ameliorates endometrial fibrosis by priming MSCs to secrete C1INH

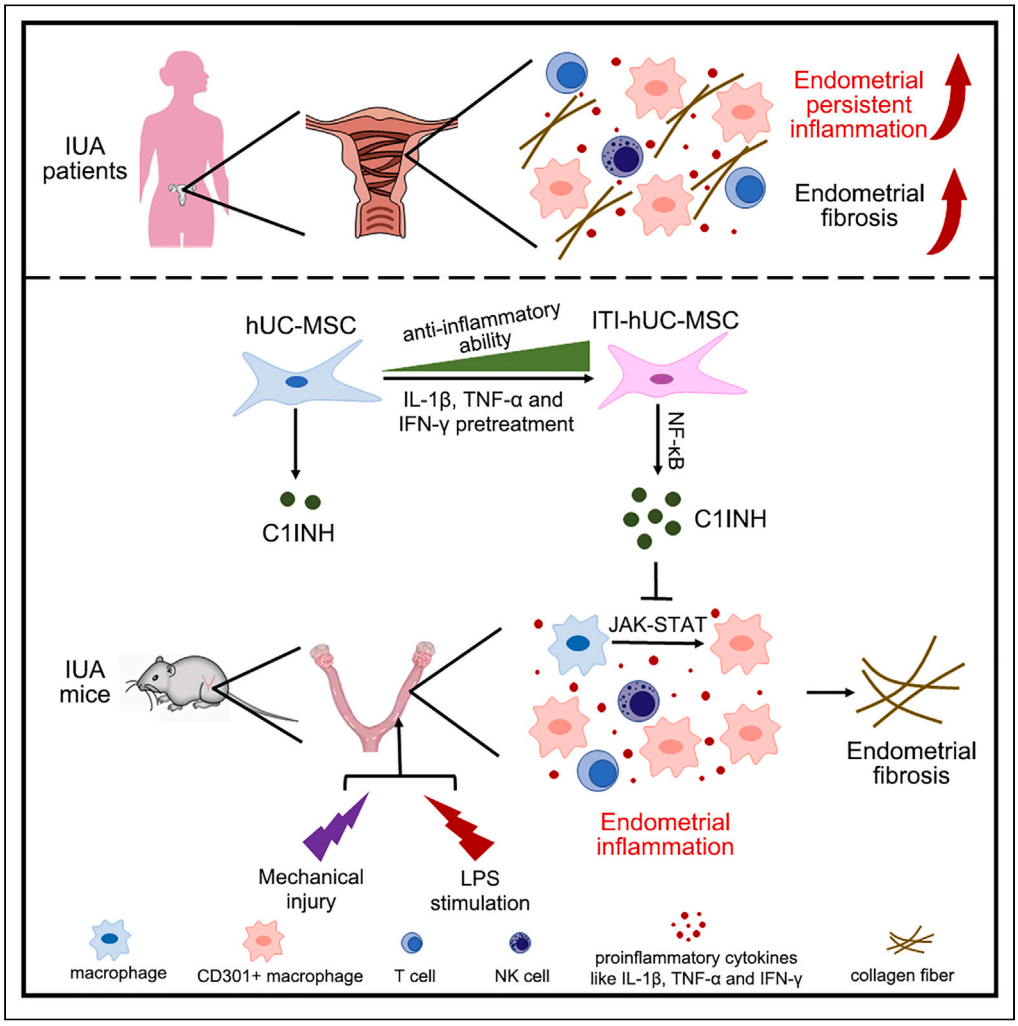

Simin Yao, Zhenhua Zhou, Limin Wang, ..., Xiwen Zhang, Guangfeng Zhao, Yali Hu

zhaoguangfeng@nju.edu.cn (G.Z.)
yalihu@nju.edu.cn (Y.H.)

Highlights

Persistent inflammation coexists with fibrosis in the endometria of IUA patients

Endometrial inflammation and its induction of CD301+ macrophages drive fibrosis

ITI-hUC-MSCs decrease endometrial inflammation and CD301+ macrophages in IUA mice

C1INH mediates ITI-hUC-MSCs' anti-inflammation to improve endometrial fibrosis

Yao et al., iScience 26, 107201
July 21, 2023 © 2023 The Author(s).
https://doi.org/10.1016/j.isci.2023.107201

iScience

CellPress
OPEN ACCESS

Article

Targeting endometrial inflammation in intrauterine adhesion ameliorates endometrial fibrosis by priming MSCs to secrete C1INH

Simin Yao,[1] Zhenhua Zhou,[1] Limin Wang,[1] Haining Lv,[1] Dan Liu,[1] Qi Zhu,[1] Xiwen Zhang,[1] Guangfeng Zhao,[1,*] and Yali Hu[1,2,*]

SUMMARY

Intrauterine adhesion (IUA) is a common cause of uterine infertility and its histopathologic characteristic is endometrial fibrosis. A shortage of stem cells in the endometrial basalis has been recognized as a common cause of IUA development because approximately 90% of patients suffer from IUA after endometrial injury. In this study, we provide evidence that persistent inflammation is the main contributor to endometrial fibrosis in IUA patients. We further found that treating an IUA-like mouse model with ITI-hUC-MSCs (hUC-MSCs reprogrammed by IL-1β, TNF-α and IFN-γ) significantly decreased endometrial inflammation and fibrosis. Mechanistically, high levels of complement 1 inhibitor (C1INH) secreted by ITI-hUC-MSCs prevented inflammation from inducing profibrotic CD301+ macrophage polarization by downregulating the JAK-STAT signaling pathway. In conclusion, persistent inflammation in the endometria of IUA patients provides macrophage polarization with a profibrotic niche to promote endometrial fibrosis, and the powerful immunomodulatory effects of ITI-hUC-MSCs improve the immune microenvironment of endometrial regeneration.

INTRODUCTION

Intrauterine adhesion (IUA), which is the typical uterine manifestation of Asherman's syndrome, is characterized by endometrial fibrosis with partial or complete uterine cavity obliteration due to adhesion of the uterine wall.[1,2] Based on the extent of endometrial cavity obliteration, the appearance of adhesions under hysteroscopy and the patient's menstrual characteristics, IUA can be divided into mild, moderate, or severe IUA.[3] Most cases of IUA are an acquired pathological condition since approximately 90% of IUA patients develop after injury to the endometrium following surgical procedures, such as dilation and curettage (D&C),[4,5] and it has been recognized that a shortage of stem cells in the endometrial basalis is the main cause of IUA.[6,7] Trials using endometrial stem cells/progenitor cells or other kinds of adult stem cell therapy for IUA have been conducted.[8–10] We and others have reported that this adult stem cell-based therapy resulted in some beneficial outcomes in IUA patients, such as improvements in endometrial fibrosis and successfully becoming pregnant and giving birth, but most patients were still infertile.[8,9] Therefore, it is important to deepen our understanding of the pathological changes in the endometrial microenvironment in IUA patients to examine effective treatments for IUA. In studies of organ fibrosis development, such as idiopathic pulmonary fibrosis and liver cirrhosis, it is accepted that inflammation participates in and even triggers tissue fibrosis.[11–13] However, the inflammatory conditions of the endometrium in IUA patients remain unclear.

In contrast to other human tissues, the endometrium experiences up to 400 cycles of proliferation, decidualization, breakdown and regeneration in a woman's reproductive lifetime.[14] Physiologically, during decidualization and menstruation, the endometrium experiences strictly controlled inflammation, and the immune cells in the endometrium play important roles in endometrial homeostasis.[14–16] We and others have reported that there are many kinds of immune cells in the human endometrium, including macrophages, T cells, B cells and NK cells,[17,18] and macrophages constitute approximately 10% of the total leukocyte population in the proliferative phase of the human endometrium; influx largely occurs in the menstrual period to quickly clear tissue debris to avoid persistent inflammation, ultimately achieving scarless healing of the endometrium.[19,20] Macrophages are malleable depending on their environment,[21–26] and our

[1]Department of Obstetrics and Gynecology, Nanjing Drum Tower Hospital, Affiliated Hospital of Medical School, Nanjing University, Nanjing, China

[2]Lead contact

*Correspondence: zhaoguangfeng@nju.edu.cn (G.Z.), yalihu@nju.edu.cn (Y.H.)

https://doi.org/10.1016/j.isci.2023.107201

This is an open access article under the CC BY-NC-ND license (http://creativecommons.org/licenses/by-nc-nd/4.0/).

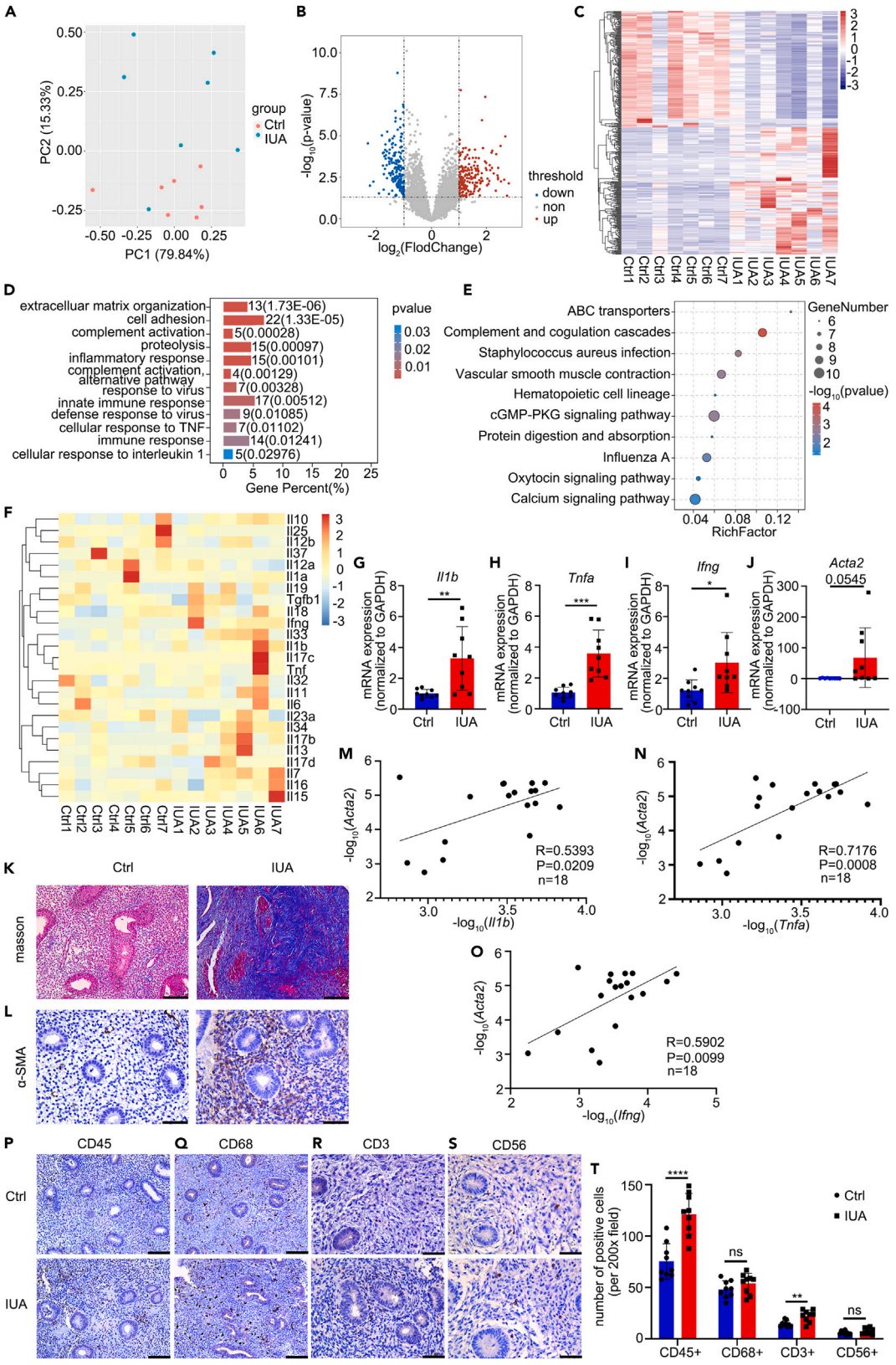
A
PC2 (15.33%)
PC1 (79.84%)
group
Ctrl
IUA
B
-log10(p-value)
log2(FlodChange)
threshold
down
non
up
C
Ctrl1 Ctrl2 Ctrl3 Ctrl4 Ctrl5 Ctrl6 Ctrl7 IUA1 IUA2 IUA3 IUA4 IUA5 IUA6 IUA7
D
extracellular matrix organization 13(1.73E-06)
cell adhesion 22(1.33E-05)
complement activation 5(0.00028)
proteolysis 15(0.00097)
inflammatory response 15(0.00101)
complement activation, alternative pathway 4(0.00129)
response to virus 7(0.00328)
innate immune response 17(0.00512)
defense response to virus 9(0.01085)
cellular response to TNF 7(0.01102)
immune response 14(0.01241)
cellular response to interleukin 1 5(0.02976)
pvalue
Gene Percent(%)
E
ABC transporters
Complement and cogulation cascades
Staphylococcus aureus infection
Vascular smooth muscle contraction
Hematopoietic cell lineage
cGMP-PKG signaling pathway
Protein digestion and absorption
Influenza A
Oxytocin signaling pathway
Calcium signaling pathway
GeneNumber
-log10(pvalue)
RichFactor
F
Il10 Il25 Il12b Il37 Il12a Il1a Il19 Tgfb1 Il18 Ifng Il33 Il1b Il17c Tnf Il32 Il11 Il6 Il23a Il34 Il17b Il13 Il17d Il7 Il16 Il15
Ctrl1 Ctrl2 Ctrl3 Ctrl4 Ctrl5 Ctrl6 Ctrl7 IUA1 IUA2 IUA3 IUA4 IUA5 IUA6 IUA7
G
Il1b
mRNA expression (normalized to GAPDH)
Ctrl IUA
H
Tnfa
I
Ifng
J
Acta2
0.0545
M
-log10(Acta2)
-log10(Il1b)
R=0.5393
P=0.0209
n=18
N
-log10(Tnfa)
R=0.7176
P=0.0008
n=18
O
-log10(Ifng)
R=0.5902
P=0.0099
n=18
K
Ctrl
IUA
masson
L
α-SMA
P
CD45
Q
CD68
R
CD3
S
CD56
Ctrl
IUA
T
number of positive cells (per 200x field)
CD45+ CD68+ CD3+ CD56+
ns

Figure 1. Aberrant inflammatory activation exists in the endometria of IUA

(A) PC (principal components) analysis of bulk RNA-seq data of endometria of severe IUA patients (n = 7) and controls (n = 7).

(B) Volcano plot of DEGs (differentially expressed genes) in the endometria of severe IUA patients (n = 7) and controls (n = 7). The red dots represent the upregulated transcripts, and the blue dots represent the downregulated transcripts ($p < 0.05$ and fold change >2).

(C) Heatmap of DEGs in the endometria of severe IUA patients (n = 7) and controls (n = 7).

(D and E) Major enriched GO biological processes and KEGG analysis of the upregulated DEGs.

(F) Heatmap of the inflammation-related genes in the endometria of severe IUA patients (n = 7) and controls (n = 7).

(G–J) The mRNA levels of *Il1b, Tnfa, Ifng* and *Acta2* in the endometria of normal controls (n = 9) and IUA patients (n = 9) measured by qRT−PCR.

(K and L) Masson's trichrome staining (scale bars: 100 μm) and immunohistochemical staining of α-SMA (scale bars: 50 μm) in the endometria of normal controls (n = 9) and IUA patients (n = 9).

(M) The correlation of $-\log_{10}$(*Acta2*) and $-\log_{10}$(*Il1b*) expression in the endometria of normal controls (n = 9) and IUA patients (n = 9). Spearman's correlation coefficient R = 0.5393, p = 0.0209.

(N) The correlation of $-\log_{10}$(*Acta2*) and $-\log_{10}$(*Tnfa*) expression in the endometria of normal controls (n = 9) and IUA patients (n = 9). Spearman's correlation coefficient R = 0.7176, p = 0.0008.

(O) The correlation of $-\log_{10}$(*Acta2*) and $-\log_{10}$(*Ifng*) expression in the endometria of normal controls (n = 9) and IUA patients (n = 9). Spearman's correlation coefficient R = 0.5902, p = 0.0099.

(P–S) Immunohistochemical staining of CD45, CD68 (scale bars of CD45 and CD68: 100 μm), CD3 and CD56 (scale bars of CD3 and CD56: 50 μm) in the endometria of normal controls (n = 9) and IUA patients (n = 9).

(T) The mean number of $CD45^+$ leukocytes, $CD68^+$ macrophages, $CD3^+$ T cells and $CD56^+$ NK cells per field at a magnification of 200×. Each point represents a patient. (G-J) and (T) Error bars indicate the mean ± SD. No significant difference (ns), *p < 0.05, **p < 0.01, ***p < 0.001, ****p < 0.0001.

previous study showed that macrophage phenotypes are altered in the endometria in IUA and involved in the development of endometrial fibrosis.[27]

Mesenchymal stem cell (MSC)-based therapy has been applied to some refractory immune diseases to control inflammation, such as lupus nephritis, Crohn's disease, and rheumatoid arthritis,[28–30] and the therapeutic mechanism mainly relies on immunomodulation, resulting in a favorable immune microenvironment.[29,31] However, accumulating evidence has shown that the immunomodulatory capacity of naive MSCs is mild and limited.[32,33] To enhance MSC immunomodulatory functions, researchers developed a new method to reprogram MSCs by pretreatment with inflammatory cytokines.[31,34] However, whether primed MSCs could improve the therapeutic efficacy of common MSCs on IUA remains unknown.

In the present study, we demonstrated that persistent inflammation was present in the endometria of IUA patients, which was positively correlated with the degree of endometrial fibrosis. In an IUA-like mouse model, we showed that increased endometrial inflammation contributes to more severe endometrial fibrosis. Furthermore, we found that hUC-MSCs primed with IL-1β, TNF-α and IFN-γ (ITI-hUC-MSCs) had powerful anti-inflammatory abilities and inhibited endometrial inflammation and prevented profibrotic CD301+ macrophage polarization through the secretion of complement 1 inhibitor (C1INH) to alleviate endometrial fibrosis in the IUA-like mouse model.

RESULTS

Aberrant inflammatory activation and fibrosis coexist in the endometria of IUA patients

To understand the difference in endometrial transcriptomic profiles in severe IUA and normal controls, bulk RNA-seq was performed on endometrial biopsies from 7 severe IUA patients and 7 normal controls in the late proliferative phase of the menstrual cycle. The results showed 321 upregulated and 250 downregulated genes ($p < 0.05$; FC > 2) in severe IUA patients compared to the controls, as shown by PC (principal components) analysis (Figure 1A), a volcano plot (Figure 1B) and a heatmap of DEGs (differentially expressed genes) (Figure 1C). GO biological process enrichment analysis revealed that fibrosis-related terms, including extracellular matrix organization and cell adhesion, and inflammation-related terms, such as complement activation, inflammatory response and the immune response, were significantly associated with the upregulated genes (Figure 1D). Consistently, KEGG pathway enrichment analysis showed that genes related to vascular smooth muscle contraction and complement and coagulation cascades were significantly upregulated in IUA patients (Figure 1E). A similar result was found in the heatmap clustering analysis, which showed the upregulation of inflammation-related genes in patients with severe IUA compared to normal controls (Figure 1F). Furthermore, proinflammatory cytokines (*Il1b, Tnfa* and *Ifng*) and a fibrotic molecule (*Acta2*) were detected in the endometria of another group of 9 patients with IUA and 9 normal controls. The results confirmed that the mRNA levels of proinflammatory cytokines and fibrotic molecules were increased (Figures 1G–1J) in IUA patients. In addition, Masson's trichrome

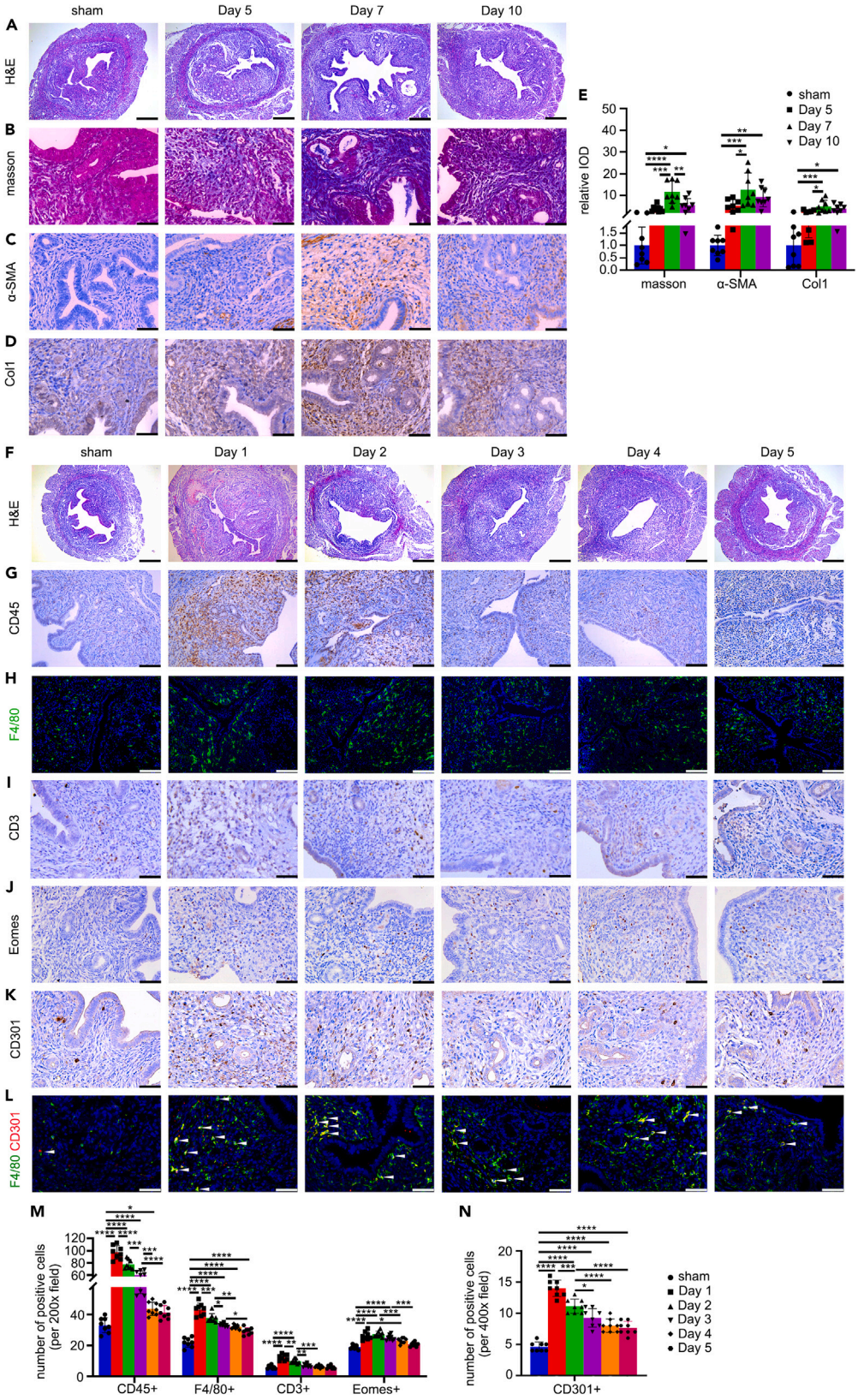
sham
Day 5
Day 7
Day 10
A
H&E
B
masson
C
α-SMA
D
Col1
E
relative IOD
masson
α-SMA
Col1
sham
Day 5
Day 7
Day 10
sham
Day 1
Day 2
Day 3
Day 4
Day 5
F
G
CD45
H
F4/80
I
CD3
J
Eomes
K
CD301
L
F4/80 CD301
M
number of positive cells (per 200x field)
CD45+
F4/80+
CD3+
Eomes+
N
number of positive cells (per 400x field)
CD301+
sham
Day 1
Day 2
Day 3
Day 4
Day 5

Figure 2. Inflammation induces changes in macrophage subtypes and the development of IUA

(A–D) H&E staining (scale bars: 200 μm), Masson's trichrome staining, and immunohistochemical staining of α-SMA and collagen 1 (scale bars of Masson, α-SMA and Col1: 50 μm) in the endometria of mice after sham operation (sham, n = 8) and on Day 5 (day 5, n = 8), Day 7 (day 7, n = 8) and Day 10 (day 10, n = 8) after modeling.

(E) The relative integrated optical density (IOD) was analyzed by Image-pro plus.

(F–K) H&E staining (scale bars: 200 μm), immunohistochemical staining of CD45, immunofluorescence analysis of F4/80 (scale bars of CD45 and F4/80: 100 μm), and immunohistochemical staining of CD3, Eomes and CD301 (scale bars of CD3, Eomes and CD301: 50 μm) in the endometria of mice after sham operation (sham, n = 8) and on Day 1 (Day 1, n = 8), Day 2 (Day 2, n = 8), Day 3 (Day 3, n = 8), Day 4 (Day 4, n = 8) and Day 5 (Day 5, n = 8) after modeling.

(L) Double immunofluorescence staining of F4/80 (green) and CD301 (red) in the endometria of mice. Scale bars: 50 μm. Arrow: F4/80+ CD301+ macrophage.

(M) The mean number of $CD45^+$ leukocytes, F4/80+ macrophages, $CD3^+$ T cells and Eomes+ NK cells per field at a magnification of 200×. Each point represents one mouse.

(N) The mean number of CD301+ macrophages per field at a magnification of 400×. Each point represents one mouse.

(E) and (M-N) Error bars indicate the mean ± SD. No significant difference (ns), *$p < 0.05$, **$p < 0.01$, ***$p < 0.001$, ****$p < 0.0001$.

(Figure 1K) and α-SMA (Figure 1L) staining were significantly elevated in the endometrial stroma of IUA patients. Correlation analysis showed that *Acta2* expression was positively correlated with the expression of *Tnfa* ($R = 0.7176$, $p < 0.01$), *Il1b* ($R = 0.5393$, $p < 0.05$) and *Ifng* ($R = 0.5902$, $p < 0.01$) in the endometria of IUA patients (Figures 1M–1O).

To understand the changes in the main immune cells in the endometria, we conducted immunohistochemical staining of CD45 (Figure 1P), CD68 (Figure 1Q), CD3 (Figure 1R) and CD56 (Figure 1S). Immunohistochemical staining of CD138 was routinely conducted by clinical pathologists for endometritis diagnosis. The results showed that the numbers of $CD45^+$ leukocytes and $CD3^+$ T cells were increased in the endometria of IUA patients compared to controls (Figure 1T), suggesting activated inflammation in the endometrium; however, no CD138-positive cells were found in the IUA patients and controls. Because macrophages play a key role in inflammation and fibrosis, we focused on macrophages. We noticed that the number of $CD68^+$ macrophages did not significantly change, but the phenotypes of macrophages were altered, and there was an increase in profibrotic CD301+ macrophages in the fibrotic endometria of IUA patients compared with controls (Figure S1), which indicated that persistent inflammatory activation was present in the fibrotic endometria of IUA patients.

Endometrial inflammation contributes to endometrial fibrosis and changes in macrophage phenotypes in the IUA-like mouse model

To investigate the effect of inflammation on macrophage differentiation and endometrial fibrosis in IUA, we compared a dual-injury mouse model (curettage plus LPS stimulation)[35] with a single-injury mouse model (curettage). More severe fibrosis was present in the endometria of mice with dual injury than in curettage only mice, indicating the important role of exacerbated inflammation in promoting endometrial fibrosis (Figure S2). Therefore, we used this dual-injury mouse model in the following experiments. As shown by H&E staining (Figure 2A), Masson's trichrome staining (Figure 2B), and α-SMA (Figure 2C) and collagen 1 (Figure 2D) immunohistochemical staining, endometrial fibrosis developed on Day 5, peaked on Day 7 and was sustained on Day 10 (Figure 2E) after modeling. However, total leukocytes ($CD45^+$), macrophages (F4/80+), T cells ($CD3^+$) and NK cells (Eomes+) were recruited to the injured sites of the uterus in the model mice, mainly on Days 1 and 2 (Figures 2F–2J and 2M) after modeling. Consistently, the mRNA levels of the proinflammatory cytokines *Il1b* and *Tnfa* were significantly increased on Day 1 after modeling, which occurred earlier than the fibrotic molecule Acta2 on Day 7 (Figure S3). Macrophages accounted for the largest proportion of leukocytes (Figure 2M), and the subtypes of macrophages were dramatically altered after modeling; there was an increase in proinflammatory and profibrotic CCR2+ (C-C motif chemokine receptor 2)[36] cells and MSR1+ (macrophage scavenger receptor 1)[37] cells (Figure S4) and especially profibrotic CD301+ macrophages (Figures 2K, 2L and 2N), which were similar to the findings in IUA patients.

ITI-hUC-MSCs relieve endometrial fibrosis induced by inflammation in the IUA-like mouse model

To examine whether inhibiting inflammation could alleviate endometrial fibrosis, we used naive MSCs and inflammatory cytokine-pretreated MSCs to inhibit endometrial inflammation and compared their anti-inflammatory and antifibrotic effects. Three cytokines (IL-1β, TNF-α and IFN-γ), were used to treat

hUC-MSCs to enhance their immunomodulatory properties. By examining the mRNA levels of the anti-inflammatory mediators *Cox2, Tsg6* and *Ido1* and the immunomodulatory factors *Il6, Il8* and *Ccl2* (Figure S5), we determined the best stimulation concentration and duration, which was 10 ng/mL IL-1β for 24 h, 20 ng/mL TNF-α for 24 h and 20 ng/mL IFN-γ for 24 h. Furthermore, we proved that the combination of these three cytokines (ITI-hUC-MSCs) exerted the best anti-inflammatory effect compared to pretreatment with one or two cytokines, as indicated by the highest mRNA and protein levels of the immunoregulatory factors IL-6, IL-8, CCL2, COX-2, TSG-6 and IDO1 (Figure 3). In contrast, cell proliferation, MSC phenotypic markers and trilineage differentiation remained unchanged in ITI-hUC-MSCs compared with hUC-MSCs (Figure S6).

Next, we randomly assigned C57BL/6J female mice into five groups, including the sham (n = 10), PBS (n = 10), Matrigel (n = 10), hUC-MSC/Matrigel (n = 10) and ITI-hUC-MSC/Matrigel (n = 10) groups, to compare the therapeutic effects of ITI-hUC-MSCs and common hUC-MSCs in IUA-like mice. As shown in the schematic diagram (Figure 4A), we injected PBS, Matrigel alone, ITI-hUC-MSCs and hUC-MSCs loaded with Matrigel into the uterus on Day 2 after modeling, whereas sham-operated mice were subjected to opening and closing of the abdominal walls, and on Days 3 and 5 after treatment, the mice were sacrificed to examine the inflammatory conditions and the severity of endometrial fibrosis, respectively. As shown by immunohistochemical staining of proinflammatory TNF-α and IL-6 and anti-inflammatory IL-10 (Figures 4B–4E), although the inflammation levels in the hUC-MSC and ITI-hUC-MSC treatment groups were significantly reduced compared with those in the PBS and Matrigel groups (Figure 4M), the lowest level of inflammation was observed in the ITI-hUC-MSC-treated group (Figures 4M and S7). Moreover, Masson's trichrome staining (Figure 4G), α-SMA staining (Figure 4H) and collagen 1 staining (Figures 4I and 4J) showed that the degree of endometrial fibrosis was the lowest in the ITI-hUC-MSC treatment group (Figures 4N and S8), although in the hUC-MSC-treated group, the degree of fibrosis was milder than that in the PBS and Matrigel only treatment groups (Figure 4N), indicating the superior effect of ITI-hUC-MSCs on inhibiting endometrial inflammation and fibrosis.

We further investigated the changes in the subtypes of macrophages in the different groups. Immunohistochemical staining revealed that the abundance of profibrotic CD301+ macrophages in the ITI-hUC-MSC group was significantly lower than that in the hUC-MSC, PBS and Matrigel groups (Figures 4K and 4O), and this trend was consistent with the degree of endometrial fibrosis. Immunofluorescence staining also confirmed that CD301 colocalized with F4/80, and the proportion of CD301+ F4/80+ cells was the lowest in the ITI-hUC-MSC group (Figure 4L). Furthermore, the proportions of CCR2+ (Figure S9A) and MSR1+ (Figure S9B) macrophages were decreased in the ITI-hUC-MSC group compared with the hUC-MSC, PBS and Matrigel groups but to a lesser extent than CD301+ macrophages. The expression levels of CD206 (Figure S9C), CD163 (Figure S9D) and CD86 (Figure S9E) were not different between the ITI-hUC-MSC and hUC-MSC groups (Figure S9F). Overall, CD301+ macrophages may be the target cells of ITI-hUC-MSC-mediated inhibition of endometrial inflammation and fibrosis.

ITI-hUC-MSC-secreted C1INH reversed inflammation-induced CD301+ macrophage polarization

To understand the underlying mechanisms by which ITI-hUC-MSCs decreased CD301+ macrophages more significantly than common hUC-MSCs *in vivo*, we further examined CD301+ macrophage polarization *in vitro*. Human THP-1 cells were induced with PMA to differentiate into naive macrophages,[38,39] which were then stimulated with LPS (100 ng/mL) and IFN-γ (20 ng/mL) to mimic the inflammatory microenvironment. Consistently, LPS and IFN-γ enhanced the proportion of CD301+ macrophages, and the mean fluorescence intensity (MFI) of CD301 was higher than that in the unstimulated group, which could be reversed by coculture with the supernatant of hUC-MSCs and ITI-hUC-MSCs; however, ITI-hUC-MSCs induced fewer CD301+ macrophages than hUC-MSCs (Figures 5A, 5B and S10A).

To identify the potential molecules by which ITI-hUC-MSCs mediate macrophage polarization, we compared the transcript profiles of ITI-hUC-MSCs and hUC-MSCs and found 811 upregulated and 1340 downregulated DEGs (FDR <0.05; FC > 2) in ITI-hUC-MSCs, as shown in the DEG heatmap (Figure 5C) and volcano plot (Figure 5D). We screened the top 200 genes by FC, top 200 genes by FDR and top 200 genes by expression abundance among these 811 genes and performed Venn analysis of the top three 200 genes to determine the most significantly upregulated genes in ITI-hUC-MSCs (Figure 5E). Finally, 43 genes were filtered out through Venn analysis (Figure 5F), and the top 10 genes by FC were *C15orf48, Cxcl5, Il32, Psmb9, Mmp3, Oas2, Serpinb2, Ifi44L, Serping1 (C1INH)* and *Cd274*. We focused

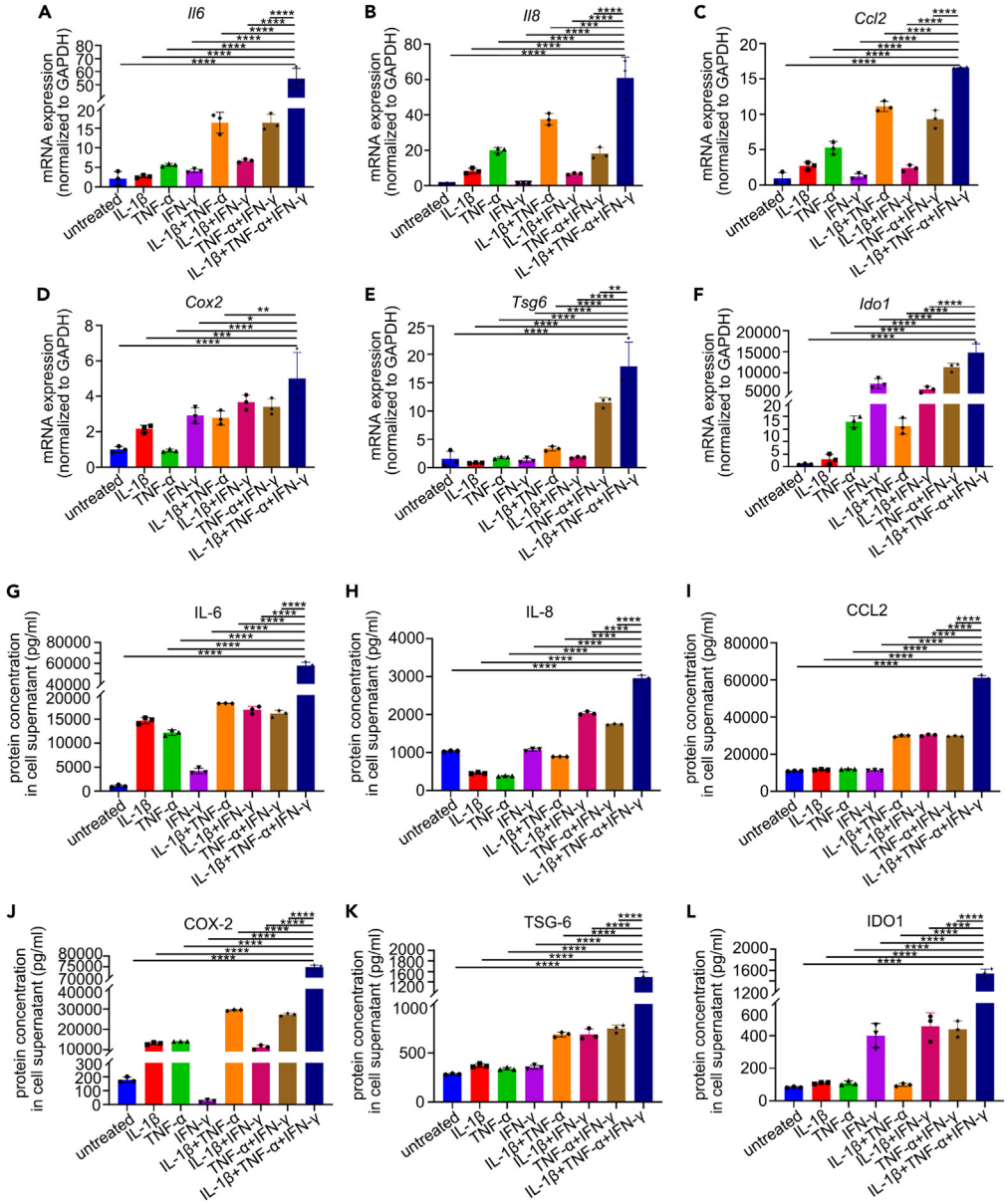

Figure 3. Inflammatory cytokine pretreatment enhances the immunomodulatory properties of hUC-MSCs

(A–F) The mRNA levels of *Il6, Il8, Ccl2, Cox2, Tsg6* and *Ido1* in hUC-MSCs that were untreated (n = 3) and treated with IL-1β (n = 3), TNF-α (n = 3), IFN-γ (n = 3), IL-1β+TNF-α (n = 3), IL-1β+IFN-γ (n = 3), TNF-α+IFN-γ (n = 3) and IL-1β+TNF-α+IFN-γ (n = 3) for 24 h were measured by qRT−PCR.

(G–L) The protein levels of IL-6, IL-8, CCL2, COX-2, TSG-6 and IDO1 in the supernatants of hUC-MSCs that were untreated (n = 3) and treated with IL-1β (n = 3), TNF-α (n = 3), IFN-γ (n = 3), IL-1β+TNF-α (n = 3), IL-1β+IFN-γ (n = 3), TNF-α+IFN-γ (n = 3) and IL-1β+TNF-α+IFN-γ (n = 3) for 24 h were detected by ELISA kits. Error bars indicate the mean ± SD. No significant difference (ns), *p < 0.05, **p < 0.01, ***p < 0.001, ****p < 0.0001.

on *Cxcl5, Il32, Mmp3* and *Serping1 (C1INH)*, which encode secreted proteins and have been reported to be involved in the inflammatory process,[40–44] and we verified their upregulation at the mRNA level by qRT−PCR (Figure 5G). The increase in C1INH (encoded by *Serping1*) at the protein level was also confirmed by western blotting (Figures 5H and 5I). Subsequently, recombinant CXCL5, IL-32β, IL-32γ, MMP3 and C1INH proteins were used to treat CD301+ macrophages induced by LPS and IFN-γ. Flow cytometry showed that only C1INH significantly reversed CD301+ macrophage polarization (Figures 5J, 5K and

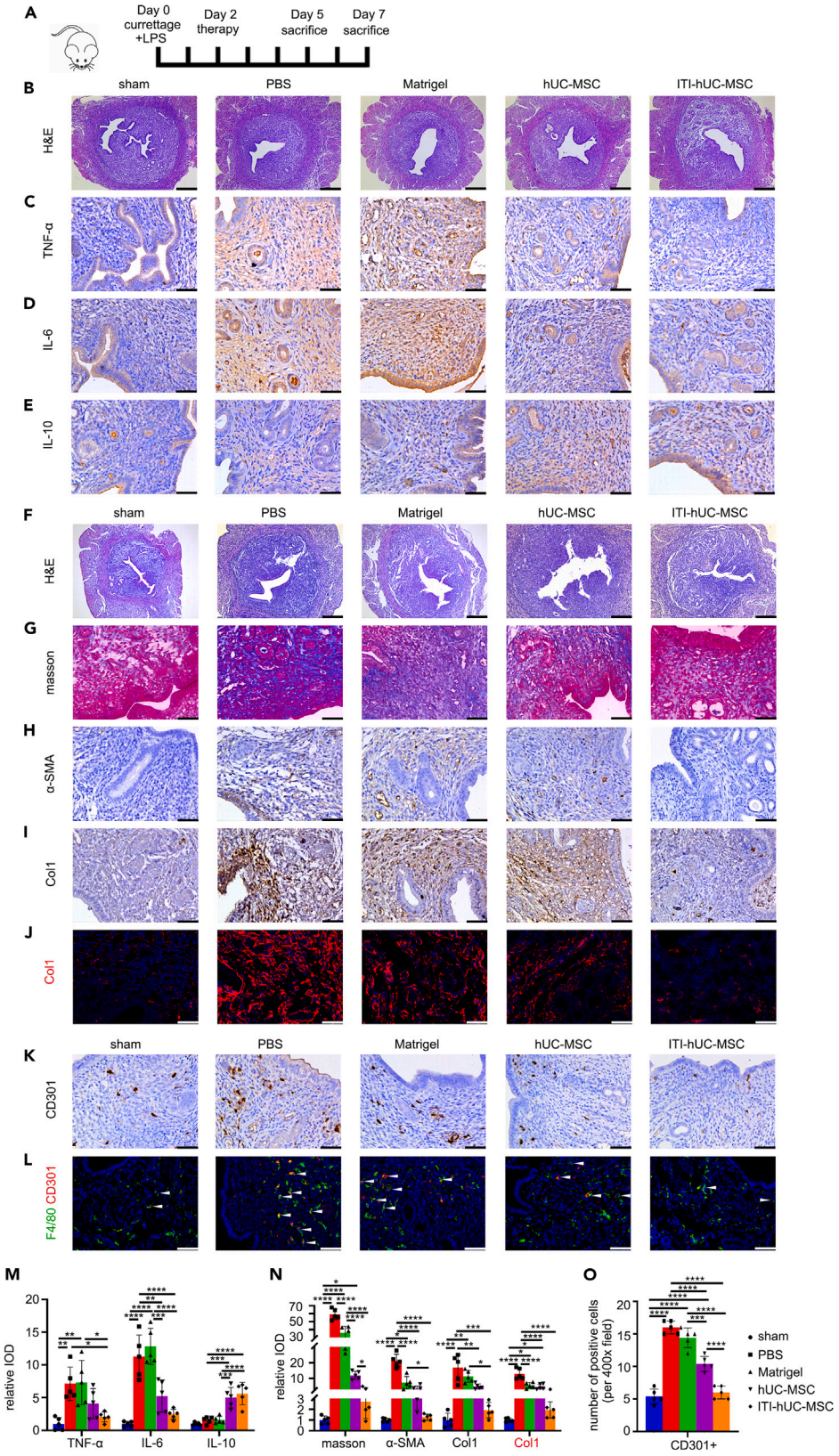
A
Day 0
currettage
+LPS
Day 2
therapy
Day 5
sacrifice
Day 7
sacrifice
B
sham
PBS
Matrigel
hUC-MSC
ITI-hUC-MSC
H&E
C
TNF-α
D
IL-6
E
IL-10
F
G
masson
H
α-SMA
I
Col1
J
K
CD301
L
F4/80 CD301
M
relative IOD
TNF-α
IL-6
IL-10
N
masson
α-SMA
Col1
O
number of positive cells
(per 400x field)
CD301+
sham
PBS
Matrigel
hUC-MSC
ITI-hUC-MSC

Figure 4. ITI-hUC-MSCs relieve endometrial inflammation and fibrosis in the IUA-like mouse model

(A) Schematic diagram of the animal experiments. The mice were divided into the following five groups: sham operation (n = 10), curettage + LPS + PBS treatment (n = 10), curettage + LPS + Matrigel treatment (n = 10), curettage + LPS + hUC-MSC/Matrigel treatment (n = 10) and curettage + LPS + ITI-hUC-MSC/Matrigel treatment (n = 10). Five mice from each group were sacrificed on Day 5 after modeling, and the others were sacrificed on Day 7 after modeling.

(B–E) H&E staining (scale bars: 200 μm) and immunohistochemical staining of TNF-α, IL-6 and IL-10 (scale bars: 50 μm) in the endometria of mice on Day 5 (n = 5) after modeling.

(M) The relative integrated optical density (IOD) was analyzed by Image-pro plus. Each point represents one mouse.

(F–J) H&E staining (scale bars: 200 μm), Masson's trichrome staining, immunohistochemical staining of α-SMA and collagen 1, and immunofluorescence analysis of collagen 1 (scale bars of Masson, α-SMA and Col1: 50 μm) in the endometria of mice on Day 7 (n = 5) after modeling.

(N) The relative integrated optical density (IOD) was analyzed by Image-pro plus. Each point represents one mouse.

(K and L) Immunohistochemical staining of CD301 and double immunofluorescence analysis of F4/80 (green) and CD301 (red) in the endometria of mice on Day 5 (n = 5) after modeling. Scale bars: 50 μm. Arrow: F4/80+ CD301+ macrophage.

(O) The mean number of CD301+ macrophages per field at a magnification of 400×. Each point represents one mouse.

(M–O) Error bars indicate the mean ± SD. No significant difference (ns), *p < 0.05, **p < 0.01, ***p < 0.001, ****p < 0.0001.

S10J), while IL-32γ slightly decreased it (Figures S10H–S10I), and CXCL5, IL-32β and MMP3 had no effect on CD301+ macrophage polarization (Figures S10B–S10G).

To investigate the critical role of C1INH in ITI-hUC-MSC-mediated inhibition of CD301+ macrophage polarization, we performed C1INH knockdown in ITI-hUC-MSCs. The results showed that all three interference sequences (si-1, si-2 and si-3) significantly suppressed the mRNA and protein expression of C1INH after transfection for 48 h (Figures 5L–5N). Among them, si-2 was the most efficient siRNA, which reduced the mRNA level to 29.63% and the protein level to 37.23% (Figures 5L–5N). Therefore, we chose si-2 for the following experiments. After downregulating C1INH, the effect of ITI-hUC-MSC conditioned media on reducing CD301+ macrophage polarization was reversed (Figures 5O and 5P), indicating that C1INH was indispensable for ITI-hUC-MSC-mediated inhibition of CD301+ macrophage polarization.

To determine the mechanisms mediating the increase in C1INH secretion in ITI-hUC-MSCs, we performed KEGG pathway analysis of the DEGs between ITI-hUC-MSCs and hUC-MSCs. Figure S11A shows the top 10 pathways, and among them, the NF-κB signaling pathway changed significantly, which is universally accepted to be involved in different inflammation-related responses. Furthermore, western blotting showed that the protein levels of p-p65 were significantly upregulated in ITI-hUC-MSCs compared with hUC-MSCs (Figures S11B and S11C), confirming the activation of the NF-κB signaling pathway. To validate the critical role of the NF-κB signaling pathway in mediating C1INH upregulation, we used a selective NF-κB inhibitor (JSH-23) to treat ITI-hUC-MSCs. As shown in Figures S11D and S11E, JSH-23 (20 μM) inhibited the protein expression of p-p65 and C1INH, suggesting that the increase in C1INH in ITI-hUC-MSCs compared with hUC-MSCs was partly dependent on the NF-κB signaling pathway.

C1INH inhibited CD301+ macrophage polarization by inhibiting the JAK-STAT signaling pathway

To investigate the pathway mediating CD301+ macrophage polarization, we sorted macrophages in the mouse endometria with F4/80 magnetic beads and analyzed the bulk RNA-seq data of macrophages in sham-operated mice and Matrigel-treated mice, in which the proportion of CD301+ macrophages was significantly increased. As shown in Figures 6A and 6B, several classic pathways, including the NF-κB, JAK-STAT, PI3K-Akt and MAPK signaling pathways, were significantly up- or downregulated in the Matrigel-treated group compared with the sham group. Furthermore, we examined the changes in these pathways *in vitro* and found that the protein levels of p-STAT1 and p-STAT3 were significantly upregulated after LPS and IFN-γ stimulation and were reversed by C1INH treatment, which was consistent with the change in CD301+ macrophages (Figures 6C and 6D). Moreover, the NF-κB, PI3K-Akt and MAPK signaling pathways showed slight changes (Figures S12A–S12C and S12H). Therefore, we hypothesized that the JAK-STAT signaling pathway plays an important role in CD301+ macrophage polarization.

To further analyze the critical role of the JAK-STAT signaling pathway in CD301+ macrophage polarization, we used a selective STAT1 phosphorylation inhibitor (fludarabine), a selective STAT3 phosphorylation inhibitor (Stattic) and a JAK1/2 phosphorylation inhibitor (ruxolitinib) to treat CD301+ macrophages induced by LPS and IFN-γ. The final concentrations of fludarabine, Stattic and ruxolitinib were 0.5 μM, 2.5 μM and

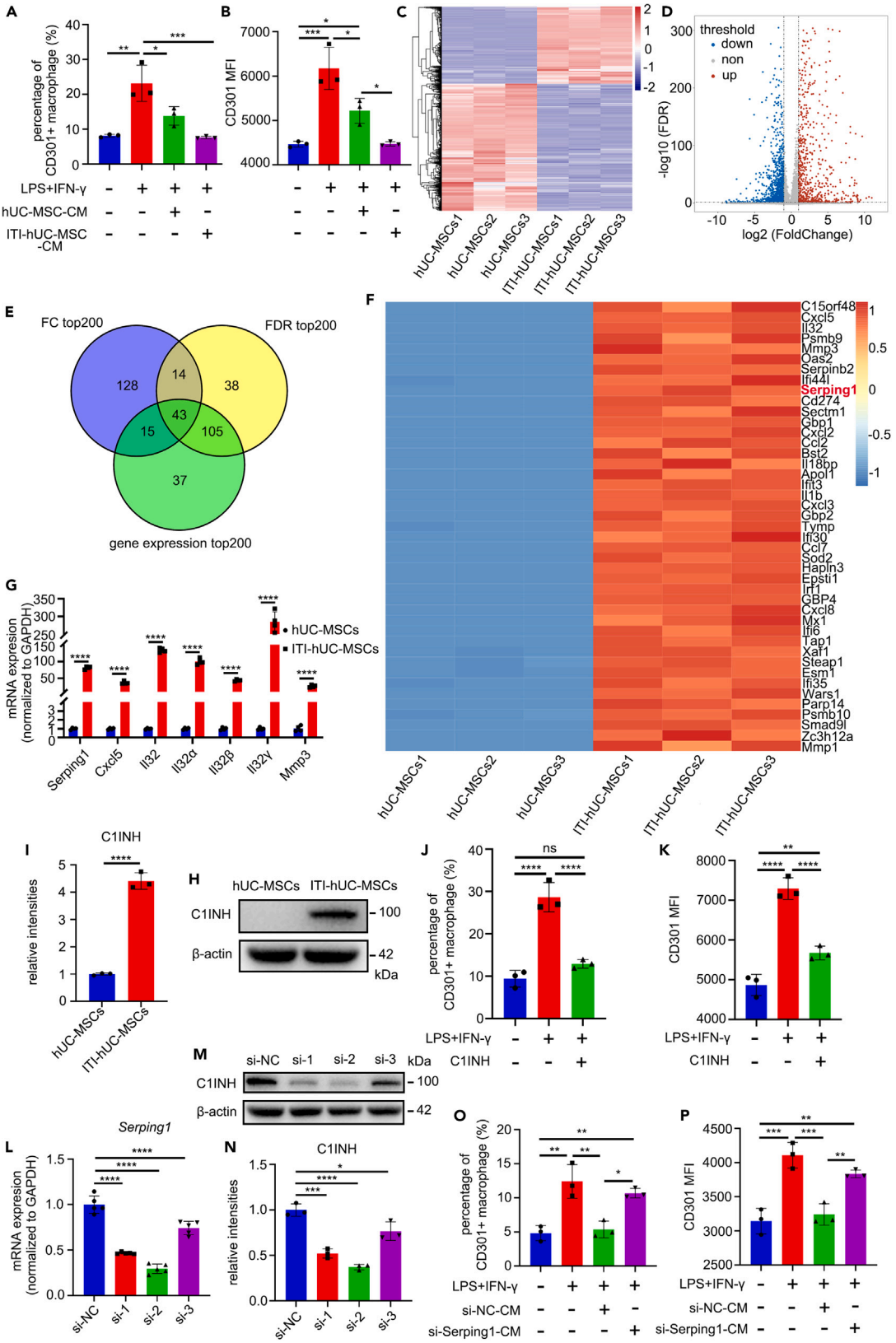
A
percentage of CD301+ macrophage (%)
LPS+IFN-γ
hUC-MSC-CM
ITI-hUC-MSC -CM
B
CD301 MFI
C
hUC-MSCs1
hUC-MSCs2
hUC-MSCs3
ITI-hUC-MSCs1
ITI-hUC-MSCs2
ITI-hUC-MSCs3
D
threshold
down
non
up
-log10 (FDR)
log2 (FoldChange)
E
FC top200
FDR top200
gene expression top200
128
14
38
43
15
105
37
F
C15orf48
Cxcl5
Il32
Psmb9
Mmp3
Oas2
Serpinb2
Ifi44l
Serping1
Cd274
Sectm1
Gbp1
Cxcl2
Ccl2
Bst2
Il18bp
Apol1
Ifit3
Il1b
Cxcl3
Gbp2
Tymp
Ifi30
Ccl7
Sod2
Hapln3
Epsti1
Irf1
GBP4
Cxcl8
Mx1
Ifi6
Tap1
Xaf1
Steap1
Esm1
Ifi35
Wars1
Parp14
Psmb10
Smad9l
Zc3h12a
Mmp1
G
mRNA expression (normalized to GAPDH)
hUC-MSCs
ITI-hUC-MSCs
Serping1
Cxcl5
Il32
Il32α
Il32β
Il32γ
Mmp3
H
hUC-MSCs
ITI-hUC-MSCs
C1INH
β-actin
100
42
kDa
I
C1INH
relative intensities
hUC-MSCs
ITI-hUC-MSCs
J
ns
percentage of CD301+ macrophage (%)
LPS+IFN-γ
C1INH
K
CD301 MFI
LPS+IFN-γ
C1INH
M
si-NC
si-1
si-2
si-3
kDa
C1INH
β-actin
100
42
Serping1
L
mRNA expression (normalized to GAPDH)
si-NC
si-1
si-2
si-3
N
C1INH
relative intensities
si-NC
si-1
si-2
si-3
O
percentage of CD301+ macrophage (%)
LPS+IFN-γ
si-NC-CM
si-Serping1-CM
P
CD301 MFI
LPS+IFN-γ
si-NC-CM
si-Serping1-CM

Figure 5. ITI-hUC-MSCs secrete C1INH to inhibit CD301+ macrophage polarization

(A and B) The proportion of CD301+ macrophages and mean fluorescence intensity (MFI) of CD301 in PMA-treated THP-1 cells stimulated with LPS and IFN-γ for 24 h and then treated with conditioned media (CM) from hUC-MSCs (n = 3) and ITI-hUC-MSCs (n = 3) for another 24 h was measured by flow cytometry.
(C and D) Heatmap and volcano plot showing DEGs in hUC-MSCs (n = 3) and ITI-hUC-MSCs (n = 3). The red dots represent the upregulated transcripts, and the blue dots represent the downregulated transcripts (FDR (false discovery rate) < 0.05 and fold change >2).
(E) Venn analysis of the top 200 genes by FC (fold change), top 200 genes by FDR and top 200 genes by expression abundance.
(F) Heatmap showing the 43 genes filtered out through Venn analysis.
(G) The mRNA levels of Serping1, Cxcl5, Il32, Il32α, Il32β, Il32γ and Mmp3 in hUC-MSCs (n = 4) and ITI-hUC-MSCs (n = 4) were measured by qRT−PCR.
(H) The protein level of C1INH was examined by western blotting in hUC-MSCs (n = 3) and ITI-hUC-MSCs (n = 3).
(I) The relative band intensities of C1INH were analyzed by ImageJ.
(J and K) The proportion of CD301+ macrophages and MFI of CD301 in PMA-treated THP-1 cells stimulated with LPS and IFN-γ for 24 h and treated with 100 ng/mL recombinant C1INH for another 24 h (n = 3) were measured by flow cytometry.
(L) The mRNA level of Serping1 in hUC-MSCs (n = 5) transfected with three different small interfering RNA-seq of Serping1 (si-1, si-2, si-3) or negative control (si-NC) for 48 h was examined by qRT−PCR.
(M) The protein level of C1INH in hUC-MSCs (n = 3) transfected with si-1, si-2, si-3 or si-NC for 48 h was examined by western blotting.
(N) The relative band intensities of C1INH were analyzed by ImageJ.
(O and P) The proportion of CD301+ macrophages and MFI of CD301 in PMA-treated THP-1 cells stimulated with LPS and IFN-γ for 24 h and treated with conditioned media of ITI-hUC-MSCs transfected with si-NC (n = 3) and si-Serping1 (si-2; n = 3) for another 24 h was measured by flow cytometry. (A-B), (G), (I-L) and (N-P) Error bars indicate the mean ± SD. No significant difference (ns), *p < 0.05, **p < 0.01, ***p < 0.001, ****p < 0.0001.

2.5 μM, respectively, depending on the cell viabilities tested with the CCK-8 kit (Figures S12D–S12F). As shown in Figures 6E–6J, fludarabine, Stattic and ruxolitinib inhibited the protein levels of p-STAT1 and p-STAT3. Furthermore, the proportions of CD301+ macrophages were significantly decreased after treatment with fludarabine, Stattic and particularly ruxolitinib (Figures 6K, 6L and S12G), which was consistent with the levels of STAT1/3 phosphorylation. Overall, these inhibitor experiments confirmed that the JAK-STAT signaling pathway was necessary for CD301+ macrophage polarization.

We also tested the activation of the JAK-STAT signaling pathway in the IUA-like mouse model. The protein levels of p-STAT1 and p-STAT3 were significantly upregulated in the PBS and Matrigel groups compared with the sham group and were reversed in the ITI-hUC-MSC group (Figures 6M and 6N). In conclusion, CD301+ macrophages were polarized, which was accompanied by STAT1/3 phosphorylation, and ITI-hUC-MSCs inhibited the activation of the JAK-STAT signaling pathway to decrease the proportion of CD301+ macrophages.

DISCUSSION

Understanding the pathogenesis of IUA can aid in the search for effective treatments for patients. Although it is widely accepted that inflammation is involved in tissue fibrosis,[11–13] few scientific reports have focused on and verified the importance of inflammation in the development of IUA. Inflammation is characterized by the recruitment of inflammatory cells and the mass secretion of proinflammatory cytokines.[45] During the physiological cycle of the endometrium, the inflammatory process takes place in endometrial decidualization and menstruation when large amounts of immune cells infiltrate the endometrium and inflammatory cytokines are produced.[46,47] However, this inflammation is self-limiting, which is necessary for successful conception.[18,46,47] In this study, to avoid the interference of physiological inflammation, all endometrial specimens were specifically collected in the late proliferative phase since endometrial inflammation is low in this phase.[18] Clinical diagnosis of chronic endometritis is based on the presence of CD138-positive cells,[48] and in this study, we demonstrated that despite negative CD138 staining, inflammatory activation was present in IUA patients (Figure 1). Because the clinical diagnosis of IUA is based on observations under hysteroscopy, whereas endometrial fibrosis is based on biopsy and pathological diagnosis, it is difficult to prove the causal relationship between endometrial inflammation and fibrosis. We showed the coexistence of inflammation and fibrosis in the endometria of IUA patients and the positive correlation between the levels of inflammatory cytokines and fibrotic molecules. Then, we used animal models to compare the timing of inflammation and fibrosis through sequential sampling and the degree of endometrial fibrosis in curettage plus LPS and curettage-only mouse models to show that inflammation occurred first, fibrosis occurred later and increased endometrial inflammation worsened fibrosis.

Macrophages are an important class of immune cells that adapt to their environment and are involved in the immune response and fibrosis in various tissues and organs.[24,49,50] Previously, our single-cell sequencing study showed a significant increase in CD301+ macrophages in the endometria of IUA patients, and targeted deletion of CD301+ macrophages inhibited endometrial fibrosis and improved the outcomes of pregnancy in

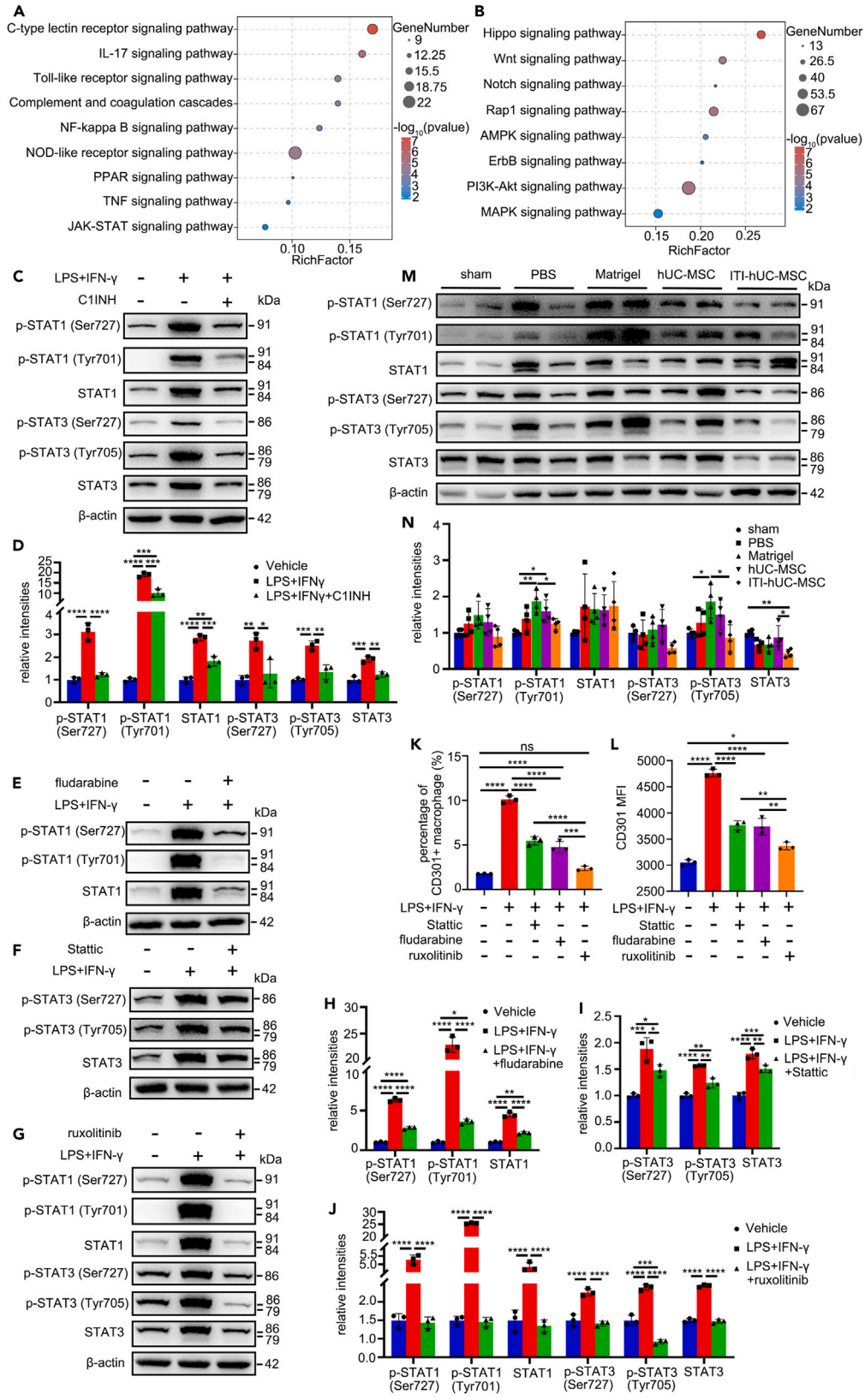
A
C-type lectin receptor signaling pathway
IL-17 signaling pathway
Toll-like receptor signaling pathway
Complement and coagulation cascades
NF-kappa B signaling pathway
NOD-like receptor signaling pathway
PPAR signaling pathway
TNF signaling pathway
JAK-STAT signaling pathway
0.10
0.15
RichFactor
GeneNumber
9
12.25
15.5
18.75
22
-log10(pvalue)
B
Hippo signaling pathway
Wnt signaling pathway
Notch signaling pathway
Rap1 signaling pathway
AMPK signaling pathway
ErbB signaling pathway
PI3K-Akt signaling pathway
MAPK signaling pathway
0.15
0.20
0.25
RichFactor
GeneNumber
13
26.5
40
53.5
67
-log10(pvalue)
C
LPS+IFN-γ
C1INH
kDa
p-STAT1 (Ser727)
p-STAT1 (Tyr701)
STAT1
p-STAT3 (Ser727)
p-STAT3 (Tyr705)
STAT3
β-actin
91
84
86
79
42
M
sham
PBS
Matrigel
hUC-MSC
ITI-hUC-MSC
kDa
p-STAT1 (Ser727)
p-STAT1 (Tyr701)
STAT1
p-STAT3 (Ser727)
p-STAT3 (Tyr705)
STAT3
β-actin
D
relative intensities
Vehicle
LPS+IFNγ
LPS+IFNγ+C1INH
p-STAT1 (Ser727)
p-STAT1 (Tyr701)
STAT1
p-STAT3 (Ser727)
p-STAT3 (Tyr705)
STAT3
N
relative intensities
sham
PBS
Matrigel
hUC-MSC
ITI-hUC-MSC
E
fludarabine
LPS+IFN-γ
kDa
p-STAT1 (Ser727)
p-STAT1 (Tyr701)
STAT1
β-actin
F
Stattic
LPS+IFN-γ
kDa
p-STAT3 (Ser727)
p-STAT3 (Tyr705)
STAT3
β-actin
G
ruxolitinib
LPS+IFN-γ
kDa
p-STAT1 (Ser727)
p-STAT1 (Tyr701)
STAT1
p-STAT3 (Ser727)
p-STAT3 (Tyr705)
STAT3
β-actin
K
ns
percentage of CD301+ macrophage (%)
LPS+IFN-γ
Stattic
fludarabine
ruxolitinib
L
CD301 MFI
LPS+IFN-γ
Stattic
fludarabine
ruxolitinib
H
relative intensities
Vehicle
LPS+IFN-γ
LPS+IFN-γ +fludarabine
p-STAT1 (Ser727)
p-STAT1 (Tyr701)
STAT1
I
relative intensities
Vehicle
LPS+IFN-γ
LPS+IFN-γ +Stattic
p-STAT3 (Ser727)
p-STAT3 (Tyr705)
STAT3
J
relative intensities
Vehicle
LPS+IFN-γ
LPS+IFN-γ +ruxolitinib
p-STAT1 (Ser727)
p-STAT1 (Tyr701)
STAT1
p-STAT3 (Ser727)
p-STAT3 (Tyr705)
STAT3

Figure 6. C1INH inhibits CD301+ macrophage polarization by inhibiting the JAK-STAT signaling pathway

(A) Major enriched pathways based on KEGG analysis of the upregulated DEGs in macrophages in the endometria of mice with curettage + LPS + Matrigel treatment (n = 3) compared with sham operation (n = 3).

(B) Major enriched pathways based on KEGG analysis of the downregulated DEGs in macrophages in the endometria of mice with curettage + LPS + Matrigel treatment (n = 3) compared with sham operation (n = 3).

(C) The protein levels of p-STAT1 (Ser727), p-STAT1 (Tyr701), STAT1, p-STAT3 (Ser727), p-STAT3 (Tyr705) and STAT3 were examined by western blotting in PMA-treated THP-1 cells that were unstimulated (n = 3) or stimulated with LPS + IFN-γ (n = 3) and LPS + IFN-γ + C1INH (n = 3).

(D) The relative band intensities were analyzed by ImageJ.

(E–G) The protein levels of p-STAT1 (Ser727), p-STAT1 (Tyr701), STAT1, p-STAT3 (Ser727), p-STAT3 (Tyr705) and STAT3 were examined by western blotting in PMA-stimulated THP-1 cells that were untreated (n = 3) or treated with LPS + IFN-γ (n = 3), LPS + IFN-γ + 0.5 μM fludarabine (n = 3), LPS + IFN-γ + 2.5 μM Stattic (n = 3) and LPS + IFN-γ + 2.5 μM ruxolitinib (n = 3) for 24 h.

(H–J) The relative band intensities were analyzed by ImageJ.

(K and L) The proportion of CD301+ macrophages and MFI of CD301 in PMA-treated THP-1 cells after treatment with LPS + IFN-γ + fludarabine (n = 3), LPS + IFN-γ + Stattic (n = 3) and LPS + IFN-γ + ruxolitinib (n = 3) for 24 h was measured by flow cytometry.

(M) The protein levels of p-STAT1 (Ser727), p-STAT1 (Tyr701), STAT1, p-STAT3 (Ser727), p-STAT3 (Tyr705) and STAT3 were examined by western blotting in the endometria of mice with sham operation (n = 4), curettage + LPS + PBS treatment (n = 4), curettage + LPS + Matrigel treatment (n = 4), curettage + LPS + hUC-MSC/Matrigel treatment (n = 4) and curettage + LPS + ITI-hUC-MSC/Matrigel treatment (n = 4) on Day 5 after modeling.

(N) The relative band intensities were analyzed by ImageJ. (D), (H-L) and (N) Error bars indicate the mean ± SD. No significant difference (ns), *p < 0.05, **p < 0.01, ***p < 0.001, ****p < 0.0001.

mice,[27] but therapies targeting CD301+ macrophages remaining unknown. In this study, we revealed that the inflammatory environment in the endometrium of IUA promoted CD301+ macrophage polarization and that applying ITI-hUC-MSCs with powerful anti-inflammatory abilities could dramatically decrease profibrotic CD301+ macrophages and endometrial inflammation and fibrosis in an IUA-like mouse model. Moreover, CCR2+ and MSR1+ macrophages, which are associated with cardiac and liver fibrosis,[36,37] were increased in the IUA-like mouse model and were slightly decreased after ITI-hUC-MSC treatment.

MSCs are present in almost all tissues and participate in tissue regeneration and homeostasis.[29,30,51–53] Increasing evidence has shown that their therapeutic effect mainly relies on immunomodulatory functions ('cell empowerment'), which could be enhanced by exposure to an inflammatory environment.[54] In this study, unlike other reports, we first used a cocktail of three cytokines (IL-1β, TNF-a and IFN-γ) to treat hUC-MSCs and found that these cells possessed stronger immunomodulatory properties than cells treated with only one or two cytokines, which provides a more effective strategy for MSC pretreatment. Furthermore, we transplanted primed human MSCs into an IUA-like mouse model to examine their immunomodulatory capacity, and we used common MSCs as controls. Immunohistochemical staining of CD3 showed that there was no difference in the abundance of T cells between the MSC treatment group and the PBS treatment group (Figure S13), excluding the effect of MSCs on tissue rejection, which is consistent with the low immunogenicity of human MSCs in animal models.[55–57] Then, animal models showed that our ITI-hUC-MSCs decreased endometrial inflammation, profibrotic CD301+ macrophage polarization and endometrial fibrosis much better than common hUC-MSCs.

To search for a therapeutic mechanism of ITI-hUC-MSCs, we first reported that ITI-hUC-MSCs could secrete a large amount of C1INH, which reversed CD301+ macrophage polarization and thereby exerted a superior effect on inhibiting endometrial inflammation and fibrosis compared to common hUC-MSCs. C1INH, which is encoded by *Serping1* and is known as C1 inhibitor, is a serpin that regulates complement and contact (kallikrein-kinin) system activation.[44] C1INH deficiency results in hereditary angioedema, which is a disease characterized by episodes of angioedema of the skin or the mucosa of the gastrointestinal tract or the oropharynx.[58,59] Recently, several reports have used recombinant C1INH protein to treat some inflammatory diseases, such as sepsis, burn wounds, peritonitis and meningitis animal models, and showed that C1INH could inhibit the inflammatory cascade, suggesting the anti-inflammatory effects of C1INH.[60–63] In this study, we identified that C1INH may reduce endometrial inflammation by inhibiting the JAK-STAT signaling pathway to inhibit CD301+ macrophage polarization.

Overall, we demonstrated that persistent inflammatory activation coexisted with fibrosis in the endometria of IUA patients and that the degree of inflammation was positively correlated with that of endometrial

fibrosis. By targeting the immune microenvironment, we proposed a new strategy for IUA treatment using cytokine-primed ITI-hUC-MSCs. Mechanistically, ITI-hUC-MSCs secreted more C1INH than common hUC-MSCs, which blocked inflammation-induced profibrotic CD301+ macrophage polarization through the JAK-STAT signaling pathway. These results provide a promising therapy for clinical patients with IUA in the future.

Limitations of the study

We have showed the positive correlation of inflammation and fibrosis in the endometria of IUA patients and the contributing role of endometrial inflammation in endometrial fibrosis of IUA mice, but the causal relationship between endometrial inflammation and fibrosis still needs further direct evidence from patients. Besides, in addition to immunomodulation, other functions, such as proangiogenesis, could also be activated by inflammatory factors[31,54] and their roles in the inhibition of endometrial fibrosis by ITI-hUC-MSCs still need further investigation.

STAR★METHODS

Detailed methods are provided in the online version of this paper and include the following:

- KEY RESOURCES TABLE
- RESOURCE AVAILABILITY
  - Lead contact
  - Materials availability
  - Data and code availability
- EXPERIMENTAL MODEL AND STUDY PARTICIPANT DETAILS
  - Animals
  - Human endometrial samples
  - Cell culture
- METHOD DETAILS
  - Cell culture and drug treatment
  - RNA isolation and quantitative real-time PCR (qRT–PCR)
  - Western blot analysis
  - Cell viability assay
  - ELISA
  - Flow cytometry
  - The trilineage differentiation of UC-MSCs
  - Experimental animal models
  - Magnetic bead sorting of macrophages
  - Histology and immunohistochemistry
  - Immunofluorescence analysis
  - Bulk RNA sequencing
- QUANTIFICATION AND STATISTICAL ANALYSIS

SUPPLEMENTAL INFORMATION

Supplemental information can be found online at https://doi.org/10.1016/j.isci.2023.107201.

ACKNOWLEDGMENTS

We thank Clinical Stem Cell Center, the Affiliated Drum Tower Hospital of Nanjing University Medical School for providing human MSCs from umbilical cord (hUC-MSCs). This study was supported by research grants from National Natural Science Foundation of China (82171618, 82071600, 82271653 and 81971336), National Key R&D Program of China (2021YFC2701603), Jiangsu Provincial Obstetrics and Gynecology Innovation Center (CXZX202229), and Jiangsu Biobank of Clinical Resources (BM2015004).

AUTHOR CONTRIBUTIONS

Conceptualization, Y.L.H. and G.F.Z.; Methodology, S.M.Y., Y.L.H., and G.F.Z.; Investigation, S.M.Y., Z.H.Z., L.M.W., H.N.L., D.L., X.W.Z., and Q.Z.; Writing – Original Draft, S.M.Y.; Writing – Review and Editing, S.M.Y., Y.L.H., and G.F.Z.; Funding Acquisition, Y.L.H. and G.F.Z.; Supervision, Y.L.H. and G.F.Z.

DECLARATION OF INTERESTS

The authors declare no competing interests.

Received: March 1, 2023
Revised: May 21, 2023
Accepted: June 20, 2023
Published: June 24, 2023

REFERENCES

1. Yu, D., Wong, Y.M., Cheong, Y., Xia, E., and Li, T.C. (2008). Asherman syndrome-one century later. Fertil. Steril. *89*, 759–779. https://doi.org/10.1016/j.fertnstert.2008.02.096.

2. AAGL Elevating Gynecologic Surgery (2017). AAGL practice report: practice guidelines on intrauterine adhesions developed in collaboration with the European Society of Gynaecological Endoscopy (ESGE). Gynecol. Surg. *14*, 6. https://doi.org/10.1186/s10397-017-1007-3.

3. (1988). The American Fertility Society classifications of adnexal adhesions, distal tubal occlusion, tubal occlusion secondary to tubal ligation, tubal pregnancies, müllerian anomalies and intrauterine adhesions. Fertil. Steril. *49*, 944–955. https://doi.org/10.1016/s0015-0282(16)59942-7.

4. Santamaria, X., Isaacson, K., and Simón, C. (2018). Asherman's Syndrome: it may not be all our fault. Hum. Reprod. *33*, 1374–1380. https://doi.org/10.1093/humrep/dey232.

5. Zupi, E., Centini, G., and Lazzeri, L. (2015). Asherman syndrome: an unsolved clinical definition and management. Fertil. Steril. *104*, 1380–1381. https://doi.org/10.1016/j.fertnstert.2015.09.036.

6. Evans, J., Salamonsen, L.A., Winship, A., Menkhorst, E., Nie, G., Gargett, C.E., and Dimitriadis, E. (2016). Fertile ground: human endometrial programming and lessons in health and disease. Nat. Rev. Endocrinol. *12*, 654–667. https://doi.org/10.1038/nrendo.2016.116.

7. Gargett, C.E., Schwab, K.E., and Deane, J.A. (2016). Endometrial stem/progenitor cells: the first 10 years. Hum. Reprod. Update *22*, 137–163. https://doi.org/10.1093/humupd/dmv051.

8. Cao, Y., Sun, H., Zhu, H., Zhu, X., Tang, X., Yan, G., Wang, J., Bai, D., Wang, J., Wang, L., et al. (2018). Allogeneic cell therapy using umbilical cord MSCs on collagen scaffolds for patients with recurrent uterine adhesion: a phase I clinical trial. Stem Cell Res. Ther. *9*, 192. https://doi.org/10.1186/s13287-018-0904-3.

9. Santamaria, X., Cabanillas, S., Cervelló, I., Arbona, C., Raga, F., Ferro, J., Palmero, J., Remohí, J., Pellicer, A., and Simón, C. (2016). Autologous cell therapy with CD133+ bone marrow-derived stem cells for refractory Asherman's syndrome and endometrial atrophy: a pilot cohort study. Hum. Reprod. *31*, 1087–1096. https://doi.org/10.1093/humrep/dew042.

10. Tan, J., Li, P., Wang, Q., Li, Y., Li, X., Zhao, D., Xu, X., and Kong, L. (2016). Autologous menstrual blood-derived stromal cells transplantation for severe Asherman's syndrome. Hum. Reprod. *31*, 2723–2729. https://doi.org/10.1093/humrep/dew235.

11. Wick, G., Grundtman, C., Mayerl, C., Wimpissinger, T.F., Feichtinger, J., Zelger, B., Sgonc, R., and Wolfram, D. (2013). The immunology of fibrosis. Annu. Rev. Immunol. *31*, 107–135. https://doi.org/10.1146/annurev-immunol-032712-095937.

12. Koyama, Y., and Brenner, D.A. (2017). Liver inflammation and fibrosis. J. Clin. Invest. *127*, 55–64. https://doi.org/10.1172/JCI88881.

13. Mack, M. (2018). Inflammation and fibrosis. Matrix Biol. *68–69*, 106–121. https://doi.org/10.1016/j.matbio.2017.11.010.

14. Kirkwood, P.M., Shaw, I.W., and Saunders, P.T.K. (2021). Mechanisms of Scarless Repair at Time of Menstruation: Insights From Mouse Models. Front. Reprod. Health *3*, 801843. https://doi.org/10.3389/frph.2021.801843.

15. Kirkwood, P.M., Gibson, D.A., Shaw, I., Dobie, R., Kelepouri, O., Henderson, N.C., and Saunders, P.T.K. (2022). Single-cell RNA sequencing and lineage tracing confirm mesenchyme to epithelial transformation (MET) contributes to repair of the endometrium at menstruation. Elife *11*, e77663. https://doi.org/10.7554/eLife.77663.

16. Spooner-Harris, M., Kerns, K., Zigo, M., Sutovsky, P., Balboula, A., and Patterson, A.L. (2023). A re-appraisal of mesenchymal-epithelial transition (MET) in endometrial epithelial remodeling. Cell Tissue Res. *391*, 393–408. https://doi.org/10.1007/s00441-022-03711-z.

17. Lv, H., Zhao, G., Jiang, P., Wang, H., Wang, Z., Yao, S., Zhou, Z., Wang, L., Liu, D., Deng, W., et al. (2022). Deciphering the endometrial niche of human thin endometrium at single-cell resolution. Proc. Natl. Acad. Sci. USA *119*, e2115912119. https://doi.org/10.1073/pnas.2115912119.

18. Wang, W., Vilella, F., Alama, P., Moreno, I., Mignardi, M., Isakova, A., Pan, W., Simon, C., and Quake, S.R. (2020). Single-cell transcriptomic atlas of the human endometrium during the menstrual cycle. Nat. Med. *26*, 1644–1653. https://doi.org/10.1038/s41591-020-1040-z.

19. Cousins, F.L., Kirkwood, P.M., Saunders, P.T.K., and Gibson, D.A. (2016). Evidence for a dynamic role for mononuclear phagocytes during endometrial repair and remodelling. Sci. Rep. *6*, 36748. https://doi.org/10.1038/srep36748.

20. Zhou, J.Z., Way, S.S., and Chen, K. (2018). Immunology of the Uterine and Vaginal Mucosae. Trends Immunol. *39*, 302–314. https://doi.org/10.1016/j.it.2018.01.007.

21. Martinez, F.O., Sica, A., Mantovani, A., and Locati, M. (2008). Macrophage activation and polarization. Front. Biosci. *13*, 453–461. https://doi.org/10.2741/2692.

22. Kim, S.Y., and Nair, M.G. (2019). Macrophages in wound healing: activation and plasticity. Immunol. Cell Biol. *97*, 258–267. https://doi.org/10.1111/imcb.12236.

23. Gao, C.C., Bai, J., Han, H., and Qin, H.Y. (2022). The versatility of macrophage heterogeneity in liver fibrosis. Front. Immunol. *13*, 968879. https://doi.org/10.3389/fimmu.2022.968879.

24. Tang, P.M.K., Nikolic-Paterson, D.J., and Lan, H.Y. (2019). Macrophages: versatile players in renal inflammation and fibrosis. Nat. Rev. Nephrol. *15*, 144–158. https://doi.org/10.1038/s41581-019-0110-2.

25. Witherel, C.E., Sao, K., Brisson, B.K., Han, B., Volk, S.W., Petrie, R.J., Han, L., and Spiller, K.L. (2021). Regulation of extracellular matrix assembly and structure by hybrid M1/M2 macrophages. Biomaterials *269*, 120667. https://doi.org/10.1016/j.biomaterials.2021.120667.

26. Kishore, A., and Petrek, M. (2021). Roles of Macrophage Polarization and Macrophage-Derived miRNAs in Pulmonary Fibrosis. Front. Immunol. *12*, 678457. https://doi.org/10.3389/fimmu.2021.678457.

27. Lv, H., Sun, H., Wang, L., Yao, S., Liu, D., Zhang, X., Pei, Z., Zhou, J., Wang, H., Dai, J., et al. (2023). Targeting CD301+ macrophage inhibits endometrial fibrosis and improves pregnancy outcome. Preprint at bioRxiv. https://doi.org/10.1101/2023.06.09.544336.

28. Hoang, D.M., Pham, P.T., Bach, T.Q., Ngo, A.T.L., Nguyen, Q.T., Phan, T.T.K., Nguyen, G.H., Le, P.T.T., Hoang, V.T., Forsyth, N.R., et al. (2022). Stem cell-based therapy for human diseases. Signal Transduct. Targeted Ther. *7*, 272. https://doi.org/10.1038/s41392-022-01134-4.

29. Shi, Y., Wang, Y., Li, Q., Liu, K., Hou, J., Shao, C., and Wang, Y. (2018). Immunoregulatory mechanisms of mesenchymal stem and stromal cells in inflammatory diseases. Nat. Rev. Nephrol. *14*, 493–507. https://doi.org/10.1038/s41581-018-0023-5.

30. Shi, Y., Su, J., Roberts, A.I., Shou, P., Rabson, A.B., and Ren, G. (2012). How mesenchymal stem cells interact with tissue immune responses. Trends Immunol. *33*, 136–143. https://doi.org/10.1016/j.it.2011.11.004.

31. Wang, Y., Chen, X., Cao, W., and Shi, Y. (2014). Plasticity of mesenchymal stem cells in immunomodulation: pathological and therapeutic implications. Nat. Immunol. *15*, 1009–1016. https://doi.org/10.1038/ni.3002.

32. Martin, I., Galipeau, J., Kessler, C., Le Blanc, K., and Dazzi, F. (2019). Challenges for mesenchymal stromal cell therapies. Sci. Transl. Med. *11*, eaat2189. https://doi.org/10.1126/scitranslmed.aat2189.

33. Ferreira, J.R., Teixeira, G.Q., Santos, S.G., Barbosa, M.A., Almeida-Porada, G., and Gonçalves, R.M. (2018). Mesenchymal Stromal Cell Secretome: Influencing Therapeutic Potential by Cellular Pre-conditioning. Front. Immunol. *9*, 2837. https://doi.org/10.3389/fimmu.2018.02837.

34. Yuan, X., Qin, X., Wang, D., Zhang, Z., Tang, X., Gao, X., Chen, W., and Sun, L. (2019). Mesenchymal stem cell therapy induces FLT3L and CD1c+ dendritic cells in systemic lupus erythematosus patients. Nat. Commun. *10*, 2498. https://doi.org/10.1038/s41467-019-10491-8.

35. Zhou, Z., Wang, H., Zhang, X., Song, M., Yao, S., Jiang, P., Liu, D., Wang, Z., Lv, H., Li, R., et al. (2022). Defective autophagy contributes to endometrial epithelial-mesenchymal transition in intrauterine adhesions. Autophagy *18*, 2427–2442. https://doi.org/10.1080/15548627.2022.2038994.

36. Revelo, X.S., Parthiban, P., Chen, C., Barrow, F., Fredrickson, G., Wang, H., Yücel, D., Herman, A., and van Berlo, J.H. (2021). Cardiac Resident Macrophages Prevent Fibrosis and Stimulate Angiogenesis. Circ. Res. *129*, 1086–1101. https://doi.org/10.1161/CIRCRESAHA.121.319737.

37. Govaere, O., Petersen, S.K., Martinez-Lopez, N., Wouters, J., Van Haele, M., Mancina, R.M., Jamialahmadi, O., Bilkei-Gorzo, O., Lassen, P.B., Darlay, R., et al. (2022). Macrophage scavenger receptor 1 mediates lipid-induced inflammation in non-alcoholic fatty liver disease. J. Hepatol. *76*, 1001–1012. https://doi.org/10.1016/j.jhep.2021.12.012.

38. Qiu, J., Shu, C., Li, X., and Zhang, W.C. (2022). PAQR3 depletion accelerates diabetic wound healing by promoting angiogenesis through inhibiting STUB1-mediated PPARγ degradation. Lab. Invest. *102*, 1121–1131. https://doi.org/10.1038/s41374-022-00786-8.

39. Han, J.L., Song, Y.X., Yao, W.J., Zhou, J., Du, Y., and Xu, T. (2023). Follicle-Stimulating Hormone Provokes Macrophages to Secrete IL-1β Contributing to Atherosclerosis Progression. J. Immunol. *210*, 25–32. https://doi.org/10.4049/jimmunol.2200475.

40. Roca, H., Jones, J.D., Purica, M.C., Weidner, S., Koh, A.J., Kuo, R., Wilkinson, J.E., Wang, Y., Daignault-Newton, S., Pienta, K.J., et al. (2018). Apoptosis-induced CXCL5 accelerates inflammation and growth of prostate tumor metastases in bone. J. Clin. Invest. *128*, 248–266. https://doi.org/10.1172/JCI92466.

41. Yan, H., Dong, M., Liu, X., Shen, Q., He, D., Huang, X., Zhang, E., Lin, X., Chen, Q., Guo, X., et al. (2019). Multiple myeloma cell-derived IL-32γ increases the immunosuppressive function of macrophages by promoting indoleamine 2,3-dioxygenase (IDO) expression. Cancer Lett. *446*, 38–48. https://doi.org/10.1016/j.canlet.2019.01.012.

42. Liu, D., Li, Q., Ding, H., Zhao, G., Wang, Z., Cao, C., Dai, Y., Zheng, M., Zhu, X., Wu, Q., et al. (2021). Placenta-derived IL-32β activates neutrophils to promote preeclampsia development. Cell. Mol. Immunol. *18*, 979–991. https://doi.org/10.1038/s41423-021-00636-5.

43. Takimoto, K., Kawashima, N., Suzuki, N., Koizumi, Y., Yamamoto, M., Nakashima, M., and Suda, H. (2014). Down-regulation of inflammatory mediator synthesis and infiltration of inflammatory cells by MMP-3 in experimentally induced rat pulpitis. J. Endod. *40*, 1404–1409. https://doi.org/10.1016/j.joen.2014.04.001.

44. Davis, A.E., 3rd, Lu, F., and Mejia, P. (2010). C1 inhibitor, a multi-functional serine protease inhibitor. Thromb. Haemostasis *104*, 886–893. https://doi.org/10.1160/TH10-01-0073.

45. Ferrucci, L., and Fabbri, E. (2018). Inflammageing: chronic inflammation in ageing, cardiovascular disease, and frailty. Nat. Rev. Cardiol. *15*, 505–522. https://doi.org/10.1038/s41569-018-0064-2.

46. Finn, C.A. (1986). Implantation, menstruation and inflammation. Biol. Rev. Camb. Phil. Soc. *61*, 313–328. https://doi.org/10.1111/j.1469-185x.1986.tb00657.x.

47. Salamonsen, L.A., and Woolley, D.E. (1999). Menstruation: induction by matrix metalloproteinases and inflammatory cells. J. Reprod. Immunol. *44*, 1–27. https://doi.org/10.1016/s0165-0378(99)00002-9.

48. Groth, J.V. (2018). Chronic endometritis and the plasma cell, fact versus fiction. Fertil. Steril. *109*, 788. https://doi.org/10.1016/j.fertnstert.2018.02.116.

49. Sly, L.M., and McKay, D.M. (2022). Macrophage immunotherapy: overcoming impediments to realize promise. Trends Immunol. *43*, 959–968. https://doi.org/10.1016/j.it.2022.10.002.

50. Guilliams, M., Thierry, G.R., Bonnardel, J., and Bajenoff, M. (2020). Establishment and Maintenance of the Macrophage Niche. Immunity *52*, 434–451. https://doi.org/10.1016/j.immuni.2020.02.015.

51. Cousins, F.L., Filby, C.E., and Gargett, C.E. (2021). Endometrial Stem/Progenitor Cells-Their Role in Endometrial Repair and Regeneration. Front. Reprod. Health *3*, 811537. https://doi.org/10.3389/frph.2021.811537.

52. Hennes, D.M.Z.B., Rosamilia, A., Werkmeister, J.A., Gargett, C.E., and Mukherjee, S. (2021). Endometrial SUSD2+ Mesenchymal Stem/Stromal Cells in Tissue Engineering: Advances in Novel Cellular Constructs for Pelvic Organ Prolapse. J. Personalized Med. *11*, 840. https://doi.org/10.3390/jpm11090840.

53. Bozorgmehr, M., Gurung, S., Darzi, S., Nikoo, S., Kazemnejad, S., Zarnani, A.H., and Gargett, C.E. (2020). Endometrial and Menstrual Blood Mesenchymal Stem/Stromal Cells: Biological Properties and Clinical Application. Front. Cell Dev. Biol. *8*, 497. https://doi.org/10.3389/fcell.2020.00497.

54. Wang, Y., Fang, J., Liu, B., Shao, C., and Shi, Y. (2022). Reciprocal regulation of mesenchymal stem cells and immune responses. Cell Stem Cell *29*, 1515–1530. https://doi.org/10.1016/j.stem.2022.10.001.

55. Wang, L., Yao, S., Huang, F., Lv, H., Liu, D., Gao, T., Wang, B., Zhou, Z., Cao, C., Zhu, Q., et al. (2023). The UCMSC-bFGF/Scaffold System Accelerates the Healing of the Uterine Full-Thickness Injury. Tissue Eng. *29*, 112–125. https://doi.org/10.1089/ten.TEA.2022.0153.

56. Xu, L., Ding, L., Wang, L., Cao, Y., Zhu, H., Lu, J., Li, X., Song, T., Hu, Y., and Dai, J. (2017). Umbilical cord-derived mesenchymal stem cells on scaffolds facilitate collagen degradation via upregulation of MMP-9 in rat uterine scars. Stem Cell Res. Ther. *8*, 84. https://doi.org/10.1186/s13287-017-0535-0.

57. Liu, L., Zhao, G., Fan, H., Zhao, X., Li, P., Wang, Z., Hu, Y., and Hou, Y. (2014). Mesenchymal stem cells ameliorate Th1-induced pre-eclampsia-like symptoms in mice via the suppression of TNF-α expression. PLoS One *9*, e88036. https://doi.org/10.1371/journal.pone.0088036.

58. Haslund, D., Ryø, L.B., Seidelin Majidi, S., Rose, I., Skipper, K.A., Fryland, T., Bohn, A.B., Koch, C., Thomsen, M.K., Palarasah, Y., et al. (2019). Dominant-negative SERPING1 variants cause intracellular retention of C1 inhibitor in hereditary angioedema. J. Clin. Invest. *129*, 388–405. https://doi.org/10.1172/JCI98869.

59. Schmaier, A.H. (2019). The hereditary angioedema syndromes. J. Clin. Invest. *129*, 66–68. https://doi.org/10.1172/JCI125378.

60. Liu, D., Zhang, D., Scafidi, J., Wu, X., Cramer, C.C., and Davis, A.E., 3rd (2005). C1 inhibitor prevents Gram-negative bacterial lipopolysaccharide-induced vascular permeability. Blood *105*, 2350–2355. https://doi.org/10.1182/blood-2004-05-1963.

61. Begieneman, M.P.V., Kubat, B., Ulrich, M.M.W., Hahn, N.E., Stumpf-Stolker, Y., Tempelaars, M.,

Middelkoop, E., Zeerleder, S., Wouters, D., van Ham, M.S., et al. (2012). Prolonged C1 inhibitor administration improves local healing of burn wounds and reduces myocardial inflammation in a rat burn wound model. J. Burn Care Res. *33*, 544–551. https://doi.org/10.1097/BCR.0b013e31823bc2fc.

62. Ozeki, T., Mizuno, M., Iguchi, D., Kojima, H., Kim, H., Suzuki, Y., Kinashi, H., Ishimoto, T., Maruyama, S., and Ito, Y. (2021). C1 inhibitor mitigates peritoneal injury in zymosan-induced peritonitis. Am. J. Physiol. Ren. Physiol. *320*, F1123–F1132. https://doi.org/10.1152/ajprenal.00600.2020.

63. Zwijnenburg, P.J.G., van der Poll, T., Florquin, S., Polfliet, M.M.J., van den Berg, T.K., Dijkstra, C.D., Roord, J.J., Hack, C.E., and van Furth, A.M. (2007). C1 inhibitor treatment improves host defense in pneumococcal meningitis in rats and mice. J. Infect. Dis. *196*, 115–123. https://doi.org/10.1086/518609.

STAR★METHODS

KEY RESOURCES TABLE

REAGENT or RESOURCE	SOURCE	IDENTIFIER
Antibodies		
Rabbit polyclonal anti-CD45	Abcam	Cat# ab10558; RRID:AB_442810
Rat monoclonal anti-F4/80	Abcam	Cat# ab6640; RRID:AB_1140040
Mouse monoclonal anti-CD68	Abcam	Cat# ab955; RRID:AB_307338
Rabbit monoclonal anti-CD3	Abcam	Cat# ab16669; RRID:AB_443425
Rabbit monoclonal anti-CD56	Abcam	Cat# ab75813; RRID:AB_2632384
Rabbit monoclonal anti-Eomes	Abcam	Cat# ab216870; RRID:AB_2721040
Rabbit polyclonal anti-CD301	Novus	Cat# NBP1-84591; RRID:AB_11031743
Goat polyclonal anti-CD301	R&D Systems	Cat# AF4297; RRID:AB_2248147
Rabbit monoclonal anti-CCR2	Abcam	Cat# ab273050; RRID:AB_2893307
Rabbit monoclonal anti-MSR1	Cell Signaling Technology	Cat# 98215; RRID:AB_2798781
Rabbit monoclonal anti-CD163	Abcam	Cat# ab182422; RRID:AB_2753196
Rabbit polyclonal anti-CD206	Abcam	Cat# ab64693; RRID:AB_1523910
Mouse monoclonal anti-CD86	Novus	Cat# NBP2-25208; RRID:AB_2923115
Rabbit monoclonal anti-CD86	Cell Signaling Technology	Cat# 19589; RRID:AB_2892094
Rabbit polyclonal anti-α-SMA	Abcam	Cat# ab5694; RRID:AB_2223021
Rabbit polyclonal anti-Col1	Proteintech	Cat# 14695-1-AP; RRID:AB_2082037
Mouse monoclonal anti-Col1	Abcam	Cat# ab88147; RRID:AB_2081873
Mouse monoclonal anti-TNFα	Abcam	Cat# ab1793; RRID:AB_302615
Rabbit polyclonal anti-IL-6	Abcam	Cat# ab208113; RRID:AB_2927421
Rabbit polyclonal anti-IL-10	Abcam	Cat# ab217941; RRID:AB_2847946
Goat anti-rat (Alexa Fluor 488)	Abcam	Cat# ab150157; RRID:AB_2722511
Goat anti-mouse (Rhodamine)	Jackson ImmunoResearch Labs	Cat# 115-026-003; RRID:AB_2338491
Goat anti-rabbit (Rhodamine)	Jackson ImmunoResearch Labs	Cat# 111-026-045; RRID:AB_2337934
Goat anti-mouse (FITC)	Jackson ImmunoResearch Labs	Cat# 115-095-003; RRID:AB_2338589
Donkey anti-goat (Alexa Fluor 647)	Abcam	Cat# ab150135; RRID:AB_2687955
Mouse monoclonal anti-C1INH	Proteintech	Cat# 66882-1-Ig; RRID:AB_2882214
Rabbit monoclonal anti-p-STAT1 (Ser727)	Cell Signaling Technology	Cat# 8826; RRID:AB_2773718
Rabbit monoclonal anti-p-STAT1 (Tyr701)	Cell Signaling Technology	Cat# 9167; RRID:AB_561284
Rabbit monoclonal anti-STAT1	Cell Signaling Technology	Cat# 14995; RRID:AB_2716280
Rabbit monoclonal anti-p-STAT3 (Ser727)	Cell Signaling Technology	Cat# 94994; RRID:AB_2800239
Rabbit monoclonal anti-p-STAT3 (Tyr705)	Cell Signaling Technology	Cat# 9145; RRID:AB_2491009
Mouse monoclonal anti-STAT3	Cell Signaling Technology	Cat# 9139; RRID:AB_331757
Rabbit monoclonal anti-p-p65	Cell Signaling Technology	Cat# 3033; RRID:AB_331284
Mouse monoclonal anti-p65	Cell Signaling Technology	Cat# 6956; RRID:AB_10828935
Rabbit monoclonal anti-*p*-Akt	Cell Signaling Technology	Cat# 4060; RRID:AB_2315049
Rabbit monoclonal anti-Akt	Cell Signaling Technology	Cat# 4691; RRID:AB_915783
Rabbit monoclonal anti-*p*-Erk1/2	Cell Signaling Technology	Cat# 4370; RRID:AB_2315112
Rabbit monoclonal anti-Erk1/2	Cell Signaling Technology	Cat# 4695; RRID:AB_390779
Rabbit monoclonal anti-p-p38	Cell Signaling Technology	Cat# 9211; RRID:AB_331641
Rabbit monoclonal anti-p38	Cell Signaling Technology	Cat# 9212; RRID:AB_330713
Rabbit monoclonal anti-p-JNK	Cell Signaling Technology	Cat# 4668; RRID:AB_823588

(*Continued on next page*)

Continued

REAGENT or RESOURCE	SOURCE	IDENTIFIER
Rabbit monoclonal anti-JNK	Cell Signaling Technology	Cat# 9252; RRID:AB_2250373
Goat anti-rabbit IgG	Cell Signaling Technology	Cat# 7074S; RRID:AB_2099233
Goat anti-mouse IgG	Cell Signaling Technology	Cat# 7076S; RRID:AB_330924
Anti-β-actin (HRP-conjugated β-Actin Rabbit mAb)	Abclonal	Cat# AC028; RRID:AB_2769861
Fixable Viability Stain 510	BD Bioscience	Cat# 564406; RRID:AB_2869572
Anti-human CD14-FITC	Biolegend	Cat# 301804; RRID:AB_314186
Anti-human CD301-APC	Biolegend	Cat# 354706; RRID:AB_11219389
Anti-F4/80 MicroBeads UltraPure, mouse	Miltenyi Biotec	Cat# 130-110-443; RRID:AB_2858241
Anti-human CD14-FITC	BD Bioscience	Cat# 557153; RRID:AB_396589
Anti-human CD19-FITC	BD Bioscience	Cat# 555412; RRID:AB_395812
Anti-human CD34-FITC	BD Bioscience	Cat# 555821; RRID:AB_396150
Anti-human CD45-FITC	BD Bioscience	Cat# 555482; RRID:AB_395874
Anti-human CD105-PE	BD Bioscience	Cat# 560839; RRID:AB_2033932
Anti-human CD90-PE	BD Bioscience	Cat# 555596; RID:AB_395970
Anti-human CD73-PE	BD Bioscience	Cat# 550257; RRID:AB_393561
Anti-human HLA-DR-PE	BD Bioscience	Cat# 555561, RRID:AB_395943
Biological samples		
Normal and IUA patient endometrial biopsies	Nanjing Drum Tower Hospital	N/A
Chemicals, peptides, and recombinant proteins		
Recombinant human IL-1β	R&D SYSTEMS	Cat# 201-LB-010
Recombinant human TNF-α	R&D SYSTEMS	Cat# 210-TA-020
Recombinant human IFN-γ	R&D SYSTEMS	Cat# 285-IF-100
Recombinant human C1INH	Peprotech	Cat# 130-20
Recombinant human CXCL5	Peprotech	Cat# 300-22
Recombinant human MMP3	Peprotech	Cat# 420-03
Recombinant human IL-32β	R&D SYSTEMS	Cat# 6769-IL-025
Recombinant human IL-32γ	R&D SYSTEMS	Cat# 4690-IL-025/CF
Lipopolysaccharides (LPS) from E. coli	Sigma-Aldrich	Cat# L2630
PMA	Sigma-Aldrich	Cat# P8139
Fludarabine	MedChem Express	Cat# HY-B0069
Stattic	MedChem Express	Cat# HY-13818
Ruxolitinib	MedChem Express	Cat# HY-50856
JSH-23	MedChem Express	Cat# HY-13982
Critical commercial assays		
CCK-8 Cell Counting Kit	Vazyme	Cat# A311-01/02
Human IL-6 ELISA Kit	R&D SYSTEMS	Cat# D6050
Human IL-8 ELISA Kit	Elabscience	Cat# E-EL-H6008
Human CCL2 ELISA Kit	Elabscience	Cat# E-EL-H6005
Human COX-2 ELISA Kit	Elabscience	Cat# E-EL-H1846c
Human TSG-6 ELISA Kit	SenBeiJia, Nanjing, China	N/A
Human IDO1 ELISA Kit	SenBeiJia, Nanjing, China	N/A
Deposited data		
Raw data of human endometria	This paper	GEO: GSE224093
Raw data of hUC-MSCs	This paper	GEO: GSE224190

(*Continued on next page*)

Continued

REAGENT or RESOURCE	SOURCE	IDENTIFIER
Raw data of mouse endometrial macrophages	This paper	GEO: GSE224288
Original western blot images	This paper; Mendeley Data	https://data.mendeley.com/datasets/g456rmfhvc/draft?a = 86cf.5d8c-7b00-42d4-b3c7-f57385a06293
Experimental models: Cell lines		
Human MSCs from the umbilical cord (hUC-MSCs)	Clinical Stem Cell Center of the Affiliated Drum Tower Hospital	N/A
Human THP-1 cell line	Cell Bank at the China Academy of Science	TCHu 57 RRID:CVCL_0006
Experimental models: Organisms/strains		
Mouse:C57BL/6J	Animal Center of Nanjing Medical University	N/A
Oligonucleotides		
qPCR Primers (See Table S2)	This paper	N/A
Recombinant DNA		
siRNA targeting Serping1	Guangzhou RiboBio Co., Ltd.	stB0002404B
Software and algorithms		
Prism version 8.0	GraphPad Software Inc	RRID:SCR_002798
ImageJ	NIH	RRID:SCR_003070
Image-Pro Plus	NIH	RRID:SCR_007369
DESeq2	R package	N/A
Other		
Matrigel	Corning Inc.	Cat# 356231
Trypsin	Wisent Inc.	Cat# 325-043-EL
Type I collagenase	Sigma-Aldrich	Cat# C0130

RESOURCE AVAILABILITY

Lead contact

Further information and requests for resources and reagents should be directed to and will be fulfilled by the lead contact, Yali Hu (yalihu@nju.edu.cn).

Materials availability

This study did not generate new unique reagents.

Data and code availability

- The RNA sequencing data have been deposited in GEO website and are publicly available as of the date of publication. Accession numbers: GSE224093 (GEO), GSE224190 (GEO) and GSE224288 (GEO). Original western blot images have been deposited at Mendeley and are publicly available as of the date of publication. The DOI is listed in the key resources table.
- This paper does not report the original code.
- Any additional information required to reanalyze the data reported in this paper is available from the lead contact upon request.

EXPERIMENTAL MODEL AND STUDY PARTICIPANT DETAILS

Animals

Female C57BL/6J mice (8–10 weeks old) weighing about 20-22g were purchased from Animal Center of Nanjing Medical University (Nanjing, China). The animals were housed in a temperature and

humidity-controlled room with a 12-day/night cycle and free access to food and water. All animal procedures were approved by the Ethics Review Board for Animal Studies of the Affiliated Drum Tower Hospital of Nanjing University (No. 2020AE01087).

Human endometrial samples

This study was approved by the Ethics Committee of Nanjing Drum Tower Hospital (No. 2012022), and informed consent was obtained from each participant. Endometrial biopsies were collected from 7 patients with severe IUA and 7 normal controls (14 Asian females, age 27–37, for details see Table S1) for bulk RNA sequencing analysis during hysteroscopy for infertility screening in the late proliferative phase of the menstrual cycle. The late proliferative phase was defined based on a follicle size between 15 and 18 mm by ultrasonography and a low level of serum progesterone. The diagnosis of severe IUA was based on the criteria recommended by the American Fertility Society. In parallel, endometria from 9 controls and 9 IUA patients were collected for further mRNA extraction and immunohistochemistry (18 Asian females, age 25–37, for details see Table S1).

Cell culture

Human MSCs from the umbilical cord (hUC-MSCs) were a kind gift from the Clinical Stem Cell Center of the Affiliated Drum Tower Hospital of Nanjing University Medical School, Nanjing. hUC-MSCs were maintained in LG-DMEM (Gibco, USA) supplemented with 10% (v/v) fetal bovine serum (FBS; Gibco, USA), 100 U/ml penicillin, and 0.1 mg/ml streptomycin at 37°C with 5% CO2 and were passaged when the confluence was over 90%. Cells at passages 3 to 5 were used for further manipulations. The THP-1 cell line was purchased from the Cell Bank at the China Academy of Science. THP-1 cells were cultured in RPMI 1640 medium (Gibco, USA) supplemented with 10% (v/v) fetal bovine serum, 100 U/ml penicillin and 0.1 mg/ml streptomycin at 37°C with 5% CO2.

METHOD DETAILS

Cell culture and drug treatment

Different concentrations of IL-1β (R&D system, USA), TNF-α (R&D system, USA) and IFN-γ (R&D system, USA) were used to treat hUC-MSCs for 24, 48 and 72 hours. For conditioned media collection, ITI-hUC-MSCs and common hUC-MSCs were rinsed with cold PBS and cultured in RPMI 1640 medium (Gibco, USA) supplemented with 10% (v/v) fetal bovine serum, 100 U/ml penicillin and 0.1 mg/ml streptomycin for another 24 hours. Then, the culture supernatants were centrifuged and collected for further experiments. For C1INH knockdown, hUC-MSCs were transfected with three small interfering RNAs (siRNAs) targeting Serping1 (si-Serping1-1, si-Serping1-2 and si-Serping1-3) and the normal control (si-NC) for 24 hours and then treated with IL-1β, TNF-α and IFN-γ for another 24 hours. A selective NF-κB inhibitor (JSH-23; MedChemExpress, USA) was added 1 hour prior to IL-1β, TNF-α and IFN-γ treatment, and then the cells were used for further experiments.

THP-1 cells were differentiated into cells with macrophage-like characteristics by 5 ng/mL PMA (Sigma–Aldrich, USA). Forty-eight hours later, the PMA was removed, and the cells were stimulated with 100 ng/ml LPS (Sigma–Aldrich, USA) and 20 ng/ml IFN-γ for 24 hours to polarize them into CD301+ macrophages. Conditional media from ITI-hUC-MSCs and hUC-MSCs and recombinant human C1INH (Peprotech, USA), CXCL5 (Peprotech, USA), IL-32β (R&D system, USA), IL-32γ (R&D system, USA) and MMP3 (Peprotech, USA) were added after LPS and IFN-γ treatment for another 24 hours, and then the cells were collected and used for further experiments. A selective STAT1 phosphorylation inhibitor (fludarabine; MedChemExpress, USA), a selective STAT3 phosphorylation inhibitor (Stattic; MedChemExpress, USA) and a JAK1/2 phosphorylation inhibitor (ruxolitinib; MedChemExpress, USA) were added 1 hour prior to LPS and IFN-γ treatment, and then the cells were used for further experiments.

RNA isolation and quantitative real-time PCR (qRT–PCR)

Total RNA was extracted from cells or tissues with TRIzol reagent (Tiangen, China) according to the manufacturer's instructions and measured by Nanodrop spectroscopy (Thermo Scientific, USA). The RNA (1 μg) was reverse-transcribed using a HiScript III 1st Strand cDNA Synthesis Kit (Vazyme, China). qRT–PCR amplification was performed using ChamQ SYBR® qPCR Master Mix (Vazyme, China) in a LightCycler 480 (Roche, USA). GAPDH served as an internal control for mRNA normalization. Relative mRNA expression was calculated by the $2^{-\Delta\Delta CT}$ method. All primer sequences used in this study are summarized in Table S2.

Western blot analysis

Cells or tissues were lysed in lysis buffer (Biosharp, China) supplemented with a protease inhibitor cocktail (MedChemExpress, USA) and phosphatase inhibitor cocktail (MedChemExpress, USA) and clarified by centrifugation at 12,000 × g for 20 min. The protein concentrations were determined using a Pierce BCA protein assay kit (Thermo Scientific, USA). Equal amounts of the protein lysate were separated by 10% SDS–PAGE gel, transferred onto PVDF membranes (Bio-Rad, USA), and incubated in 5% nonfat milk (Bio-Rad, USA) at room temperature. The membranes were incubated with primary antibodies at 4°C overnight and then hybridized with HRP-conjugated secondary antibodies at room temperature for 1 h. The signals were visualized with ECL solution (Bio-Rad, USA) and quantified by analyzing the integrated density, which was normalized to the level of β-actin using ImageJ software (NIH, USA). The antibodies used are shown in Table S3.

Cell viability assay

The viability of hUC-MSCs and THP-1 cells was determined using a Cell Counting Kit-8 assay (CCK-8; Vazyme, China) according to the manufacturer's protocol. Cells (2×10^4) were seeded into 96-well plates overnight and then exposed to different drug treatments. After the supernatant was removed, the cells were incubated with 200 μl of LG-DMEM or RPMI 1640 medium containing 20 μl of CCK-8 solution for an additional 2 h at 37°C and 5% CO_2. The optical density (OD) values were measured at a wavelength of 450 nm.

ELISA

hUC-MSCs were treated with different combinations of IL-1β, TNF-α and IFN-γ for 24 hours. The cell supernatants were centrifuged and collected and then analyzed by IL-6 (R&D system, USA), IL-8 (Elabscience, China), CCL2 (Elabscience, China), COX-2 (Elabscience, China), TSG-6 (SenBeiJia, China) and IDO1 ELISA kit (SenBeiJia, China) ELISA kits according to the manufacturer's protocols.

Flow cytometry

hUC-MSC and ITI-hUC-MSC surface antigens were analyzed by flow cytometry. In total, 5×10^5 detached cells were incubated with 1% bovine serum albumin (BSA)/PBS (Gibco, USA) for 30 min to block nonspecific antigens. Subsequently, the cells were incubated in the dark with fluorescein isothiocyanate (FITC)-labeled anti-CD14 (BD bioscience, USA), CD19 (BD bioscience, USA), CD34 (BD bioscience, USA), and CD45 (BD bioscience, USA) and phycoerythrin (PE)-conjugated anti-CD105 (BD bioscience, USA), CD90 (BD bioscience, USA), CD73 (BD bioscience, USA), and HLA-DR (BD bioscience, USA) at 4°C for 30 min. The cells were washed twice with 1% BSA/PBS and resuspended in 200 μl of 1% BSA/PBS. The data were acquired using CytoFLEX (Beckman Coulter, USA). Analysis was performed using CytExpert (Beckman Coulter, USA).

THP-1 cells were treated, digested with trypsin/EDTA (Gibco, USA) and centrifuged at 1500 rpm for 5 minutes. After being washed and resuspended in PBS, the cells were stained to determine viability (FVS510; BD Biosciences, USA) and with the following antibodies for 20 min at room temperature: CD14-FITC (Biolegend, USA) and CD301-APC (Biolegend, USA). All isotype-matched controls were purchased from Biolegend. The cells were washed twice with PBS and then resuspended in 200 μL of PBS. Data were acquired using CytoFLEX (Beckman Coulter, USA). Analysis was performed using CytExpert (Beckman Coulter, USA).

The trilineage differentiation of UC-MSCs

For adipogenesis induction, ITI-hUC-MSCs and common hUC-MSCs were cultured in adipogenic induction medium (HyCyte™, China) for 14~21 days and confirmed to have intracellular lipid accumulation by Oil red O staining. For osteogenic induction, ITI-hUC-MSCs and common hUC-MSCs were cultured in osteogenic induction medium (HyCyte™, China) for 14~21 days and confirmed to have calcium deposition by Alizarin red staining. For chondrogenic induction, ITI-hUC-MSCs and common hUC-MSCs were cultured in chondrogenic medium (HyCyte™, China) for approximately 21 days as a 3D sphere. Then, the cartilage sphere was fixed in 4% formaldehyde, embedded in paraffin, cut into slices, and confirmed to have cartilage differentiation by Alcian blue staining.

Experimental animal models

To establish an IUA-like mouse model, mechanical and inflammatory damage were performed at the estrum stage.[35] Briefly, after anesthetization with isoflurane inhalation, the uterus was exposed by

laparotomy. A rough-surfaced 7-gauge needle was inserted and used to carefully scratch the entire uterine wall approximately 50 times until the uterus became hyperemic, and then 10 μl of LPS (1 mg/ml; Sigma–Aldrich, USA) was injected into each uterine horn and clamped with tweezers for 5 min. Finally, the uterus was gently placed back into the abdominal cavity, and the abdomen wall was closed. The other group was subjected to curettage without LPS. Sham-operated mice underwent the same procedure without curettage or injection of LPS. To observe the development of inflammation and fibrosis, the mice were sacrificed on Days 1, 2, 3, 4, 5, 7 and 10 after the model was established. Furthermore, mice subjected to only curettage were sacrificed on Day 7 after modeling to compare the degree of endometrial fibrosis with the curettage + LPS model. The uteri were obtained for further analysis.

For cell treatment of the IUA-like mouse model, on Day 2 after modeling, the mice underwent a second laparotomy, and ITI-hUC-MSCs and hUC-MSCs (2×10^4/μl, 20 μl) loaded in Matrigel (Corning, USA) were injected into each uterine horn and clamped with tweezers for 7 min. The abdominal cavity was subsequently closed. PBS and only Matrigel (20 μl) were used as corresponding controls. Sham-operated mice underwent opening and closing of the abdominal wall. These mice were sacrificed on Days 3 and 5 after cell therapy (Days 5 and 7 after the IUA-like model was established), and the uteri were collected for further study.

Magnetic bead sorting of macrophages

Mouse endometrial tissues (on Day 3 after cell therapy) were cut into small pieces, digested with 0.1% trypsin (Wisent Inc., Canada) for 8 min and then transferred into type I collagenase (0.8 mg/mL, Sigma–Aldrich, USA) for 90 min at 37°C and 5% CO_2 with regular vigorous shaking in a humidified incubator. The released endometrial cells were filtered through a 70 μm cell strainer (BD Bioscience, USA), centrifuged and resuspended in 1 mL of red blood cell lysis buffer (eBioscience, USA) for 2 min to remove any remaining red blood cells. Then, the endometrial cells were resuspended in PBS and stained with Anti-F4/80 MicroBeads UltraPure (Miltenyi Biotec, Germany) for 15 min at 4°C. The labeled cells were washed and resuspended in MACS buffer (Miltenyi Biotec, Germany) and underwent magnetic separation with MS columns according to the manufacturer's protocol. The final sorted F4/80+ cells were collected for further bulk RNA sequencing.

Histology and immunohistochemistry

For immunohistochemistry, human and mouse endometrial tissues were fixed in 4% formaldehyde overnight and then embedded in paraffin after dehydration and hyalinization. The paraffin-embedded tissues were cut into 5-μm-thick slices and stained with hematoxylin and eosin (H&E) or Masson's trichrome according to the kit instructions (Solarbio, China). For immunohistochemical staining, the slices were dewaxed and rehydrated, endogenous peroxidase was eliminated with 3% hydrogen peroxide, and heat-mediated antigen retrieval was performed. Then, nonspecific binding sites were blocked with 2% bovine serum albumin (BSA; Biofroxx, Germany) for 30 minutes at room temperature. After this, the slides were incubated with primary antibodies at 4°C overnight and then with corresponding HRP-conjugated secondary antibodies (Typng, China; MXB, China) at room temperature for 8 or 15 minutes. The sections were then developed with 3'3-diaminobenzidine (DAB; Typng, China) to visualize the antigen signals and counterstained with hematoxylin. After being sealed with a neutral resin, the sections were viewed under a microscope (DMi8; Leica, Germany), and the integrated optical densities were quantified with Image-Pro Plus software. The antibodies used in this study are listed in Table S3.

Immunofluorescence analysis

Tissues from mouse uteri or human endometria were fixed with 4% paraformaldehyde overnight, dehydrated in graded sucrose, embedded in OCT and frozen. The OCT-embedded mouse endometrial tissues were cut into 5-μm-thick slices. The slices were permeabilized with 0.1% PBST (0.1% Triton X-100 [Solarbio, China] in PBS) and blocked with 2% BSA for 30 minutes. Then, the slices were incubated with primary antibodies overnight at 4°C and with secondary antibodies at room temperature away in the dark for 1 h. Nuclei were labeled with DAPI (Abcam, USA). Images were taken with a fluorescence microscope (DMi8; Leica, Germany) and quantified by measuring the integrated optical density using Image-Pro Plus. The antibodies used in this study are listed in Table S3.

Bulk RNA sequencing

RNA sequencing of the endometria of 7 normal and 7 severe IUA patients was performed at Vazyme Biotech Co. (Nanjing, China). Total RNA was extracted by an RNeasy Plus Micro Kit (Qiagen, Germany).

RNA quality was checked using 1% agarose gel electrophoresis and an RNA Nano 6000 Assay Kit (Agilent, USA).

Transcriptome sequencing analysis of *in vitro* hUC-MSCs and sorted F4/80+ mouse macrophages was performed on an Illumina HiSeq4000 by Gene Denovo Biotechnology Co. (Guangzhou, China). Total RNA was extracted using TRIzol reagent. RNA quality was assessed on an Agilent 2100 Bioanalyzer (Agilent Technologies, USA) and RNase-free agarose gel electrophoresis.

Differential expression analysis between two different groups was performed with DESeq2 software. Genes with a false discovery rate (FDR) or p value less than 0.05 and absolute fold change (FC) greater than 2 were considered differentially expressed genes (DEGs). Gene Ontology (GO) biological process enrichment analysis and KEGG pathway enrichment analysis were performed for all DEGs with the DAVID Functional Annotation Tool (https://david.ncifcrf.gov/).

QUANTIFICATION AND STATISTICAL ANALYSIS

Statistical analysis was performed using GraphPad Prism Version 8 (GraphPad Software, USA) software, and the results are presented as the means ± standard deviation (SD) or means ± standard error of the means (SEM) of at least three independent experiments. Differences between two groups were analyzed using Student's t test, and differences among three or more groups were analyzed using one-way ANOVA followed by a Student-Newman–Keuls multiple comparisons test. A P value < 0.05 was considered statistically significant.